



**HAL**  
open science

## High-resolution air-sea coupling impact on two heavy precipitation events in the Western Mediterranean

Romain Rainaud, C. Lebeaupin Brossier, Vincent Ducrocq, Hervé Giordani

► **To cite this version:**

Romain Rainaud, C. Lebeaupin Brossier, Vincent Ducrocq, Hervé Giordani. High-resolution air-sea coupling impact on two heavy precipitation events in the Western Mediterranean. *Quarterly Journal of the Royal Meteorological Society*, 2017, 143 (707), pp.2448-2462. 10.1002/qj.3098 . meteo-02109267

**HAL Id: meteo-02109267**

**<https://meteofrance.hal.science/meteo-02109267v1>**

Submitted on 24 Apr 2019

**HAL** is a multi-disciplinary open access archive for the deposit and dissemination of scientific research documents, whether they are published or not. The documents may come from teaching and research institutions in France or abroad, or from public or private research centers.

L'archive ouverte pluridisciplinaire **HAL**, est destinée au dépôt et à la diffusion de documents scientifiques de niveau recherche, publiés ou non, émanant des établissements d'enseignement et de recherche français ou étrangers, des laboratoires publics ou privés.



**High-resolution air-sea coupling impact on two heavy precipitation events in the Western Mediterranean**

Journal:	<i>QJRMS</i>
Manuscript ID	QJ-16-0220.R2
Wiley - Manuscript type:	Research Article
Date Submitted by the Author:	n/a
Complete List of Authors:	Rainaud, Romain; CNRM UMR3589 LEBEAUPIN BROSSIER, Cindy; CNRM UMR3589 Ducrocq, Veronique; CNRM UMR3589 GIORDANI, Hervé; CNRM UMR3589
Keywords:	air-sea coupling, AROME, heavy precipitation events, HyMeX, mistral, NEMO



---

# High-resolution air-sea coupling impact on two heavy precipitation events in the Western Mediterranean

R. Rainaud, C. Lebeaupin Brossier\*, V. Ducrocq, H. Giordani

*Centre National de Recherches Météorologiques (CNRM) UMR 3589 (Météo-France & CNRS), Toulouse, France*

\*Correspondence to: C. Lebeaupin Brossier, CNRM, 42 Avenue G. Coriolis, 31057 Toulouse cedex, France,  
cindy.lebeaupin-brossier@meteo.fr

---

The Mediterranean Sea is an important source of heat and moisture for heavy precipitation events (HPEs). Moreover, the Ocean Mixed Layer (OML) evolves rapidly under such intense events. Whereas short-term Numerical Weather Prediction systems generally use low-resolution non-evolving Sea Surface Temperature (SST), the development of high-resolution high-frequency coupled system allows to fully take into account the fine-scale interactions between the low-level atmosphere and the OML which occur during HPEs.

The aim of this study is to investigate the impact of fine-scale air-sea interactions and coupled processes involved during the HPEs which occurred during the 12 to 15 October 2012 (IOP13) and 26 to 28 October 2012 (IOP16a/b) of the HyMeX first field campaign. For that purpose, the high-resolution coupled system AROME-NEMO WMED was developed. This system is based on the 2.5 km-resolution non-hydrostatic convection-permitting atmospheric model AROME-WMED and the 1/36°-resolution NEMO-WMED36 ocean model. The coupling frequency is 1h. To distinguish the effects due to the change in the initial SST field from that due to the interactive 3D ocean, the coupled run is compared to two AROME-WMED atmosphere-only experiments with no SST evolution during the 48-hour forecast cycles: one using the AROME-WMED SST analysis, the second using the SST field of the coupled experiment each day at 00UTC. The results of the three experiments re-assert that the SST initial condition strongly influences the HPE forecast, in terms of intensity and location. With water budget analyses, the significant impact of the ocean interactive evolution on the surface evaporation water supply for HPE is also highlighted. In case of strong and intense air-sea exchanges, like during the mistral event of IOP16b, the coupling reproduces the intense and rapid surface cooling and demonstrates the importance of representing the ocean turbulent mixing with entrainment at the OML base.

*Key Words:* air-sea coupling; AROME; heavy precipitation events; HyMeX; mistral; NEMO

*Received...*

1 **1. Introduction**

2  
3  
4 The Western Mediterranean coastal region is frequently affected  
5 together with the winds which modulate the efficiency of the  
6 by Heavy Precipitation Events (HPEs, accumulations >100  
7 exchanges. These interactions modify the low-level atmosphere  
8 mm in 24 hours), mainly during fall, which sometimes lead  
9 stability and can notably impact the intensity of atmospheric  
10 to severe damages and human casualties. Over South-Eastern  
11 convection and precipitation (e.g. Homar et al. 2003; Xie et al.  
12 France, HPEs are generally generated by Mesoscale Convective  
13 2005). The SST can influence the structure and organization  
14 Systems (MCSs) which develop eastward of an upper-level trough  
15 of precipitating systems (tropical cyclone-like, convective or  
16 (Nuissier et al. 2008, 2011) and are favoured by a low-level moist  
17 frontal systems), their life cycle, severity, propagation speed,  
18 unstable marine flow directed towards the mountainous coasts of  
19 and track, as shown by several numerical studies considering  
20 the region (Fig. 1a). The lifting mechanisms leading to quasi-  
21 the sensitivity of HPEs to SST in the Western and Central  
22 stationary MCSs generating the large rainfall amounts include  
23 Mediterranean region (e.g. Pastor et al. 2001; Lebeaupin et  
24 orographic lifting, low-level wind convergence and cold pools  
25 al. 2006; Miglietta et al. 2011; Romero et al. 2015; Stocchi  
26 due to precipitation evaporation (Ducrocq et al. 2008, 2016).  
27 and Davolio 2016). Not only the SST value, but also the SST  
28 The mountains and islands of the region induce deflection of the  
29 patterns are characteristics that have to be accounted for in  
30 flow, channelling effects, lee cyclogenesis and blocking of the  
31 HPE high-resolution modelling and forecast. In addition, during  
32 thunderstorm cold pools that act on the lifting mechanisms. These  
33 intense meteorological events in the Mediterranean, significant  
34 indirect effects of the terrain mainly result from the interaction of  
35 interactions between the Oceanic Mixed Layer (OML) and the  
36 the large-scale flow with the orography of the region (Ricard et al.  
37 low-level atmosphere can occur on short time scales of only  
38 2012). The moisture and velocity of the low-level flows, which  
39 several hours (Lebeaupin Brossier et al. 2014). Generally, the  
40 influence the deflection of the flows by islands or mountains,  
41 intense and rapid sea surface evolution which occurs at fine-  
42 making the environment more favourable to flow over/around  
43 scale is not taken into account in Numerical Weather Prediction  
44 depending on the Froude number, have been shown to have a  
45 systems. Most of the time, the ocean conditions are prescribed  
46 significant role on the location of heavy precipitation (Bresson et  
47 using only a low- to medium-resolution SST initial field which  
48 al. 2012).

49  
50 The Mediterranean area is also affected by strong regional  
51 winds, associated with low pressure systems over the region,  
52 channelled and accelerated in the steep valleys characteristic of  
53 the Mediterranean coastal area (Fig. 1b). In the North-Western  
54 Mediterranean area, the cold and dry regional winds known as  
55 mistral (northerly) and tramontane (north-westerly) frequently  
56 occur. Gusts exceeding  $100 \text{ km h}^{-1}$  are very frequent in South-  
57 Eastern France during such strong wind events and may cause  
58 substantial damages.

59  
60 The Mediterranean Sea is a significant heat and moisture source  
(Duffourg and Ducrocq 2011) and air-sea exchanges play a key  
role during these intense events (Lebeaupin Brossier et al. 2008).  
These exchanges are expressed in terms of the turbulent fluxes of  
heat, moisture and momentum, which are controlled by gradients  
of temperature, humidity and velocity at the air-sea interface.

40  
41  
42  
43  
44  
45  
46  
47  
48  
49  
50  
51  
52  
53  
54  
55  
56  
57  
58  
59  
60  
61  
62  
63  
64  
65  
66  
67  
68  
69  
70  
71  
72  
73  
74  
75  
76  
77  
78  
79

Past studies investigated the effects of coupling an ocean model  
to high-resolution atmospheric models in the context of severe  
weather short-range forecast.

Lebeaupin Brossier et al. (2009) developed the coupled system  
between the Meso-NH atmospheric model (Lafare et al. 1998) and  
the Gaspar et al. (1990) 1D ocean model to evaluate the air-sea  
coupled effects for three case studies in South-Eastern France.  
This study showed that the Mediterranean Sea loses energy to  
feed the atmospheric convection. The OML cools and deepens  
under the low-level wind jet. The interactive coupling reduces  
the atmospheric and oceanic responses compared to uncoupled  
runs. However, their conclusions are limited because of the short  
duration (18-24 hours) and small domain (around the Gulf of  
Lion) of their simulations. Moreover, using a 1D ocean model

leads to SST errors during intense events, mainly because it does not take into account the 3D ocean circulation regulating the OML evolution (Davolio et al. 2015). Pullen et al. (2006, 2007) showed that, in the Adriatic area, the 3D high-resolution (4 km) air-sea coupling, with the COAMPS (Coupled Ocean-Atmosphere Mesoscale Prediction System) model, improves the simulation of both ocean surface and low-level atmosphere during strong wind events. The ocean cooling under strong wind stabilizes the atmospheric boundary layer and reduces the heat exchanges and low-level wind. The same results were found by Small et al. (2011, 2012) in the Ligurian Sea during mistral events. The COAWST (Coupled Ocean-Atmosphere-Wave-Sediment-Transport Warner et al. 2010) coupled system was used at high resolution (up to 1 km-resolution for the atmosphere and up to 250 m-resolution for the ocean [and wave] model[s]) for several intense weather events over the Mediterranean region (Renault et al. 2012; Ricchi et al. 2016; Grifoll et al. 2016). These studies highlighted that the fully atmosphere-ocean[waves] coupling improves the simulation results mainly in terms of surface heat fluxes, but also in terms of low-level atmosphere circulation and stability and on storm intensification.

The present study aims also at better understanding and evaluating the ocean-atmosphere coupling impacts but on HPEs and in the context of short-range and high-resolution weather forecasts.

The international HyMeX (*Hydrological cycle in Mediterranean Experiment*, [www.hymex.org](http://www.hymex.org)) program (Drobinski et al. 2014) investigates the Mediterranean hydrological cycle. A large part of the program is devoted to increasing the knowledge and the prediction skill of high-impact weather events in the area. Two field campaigns, called Special Observation Periods (SOPs), were organised in autumn 2012 and winter 2013 to document intense meteorological events and their environment.

During the first SOP (SOP1, between 5 September to 6 November 2012) focusing on heavy precipitation and flash-flood events, more than 200 instruments were deployed on land, in the air and at sea over the Western Mediterranean area (Ducrocq et al. 2014). Some of these instruments were devoted to measuring air-sea exchanges and marine atmospheric and oceanic boundary

layers upstream of HPEs (*e.g.* gliders, moored and drifting buoys, CTD profiles, balloons and radio-soundings). Facilities like aircraft or ships were also used during the Intense Observation Periods (IOPs). Forecasts were used during the field campaign to support the instrument deployment in real-time. In particular, the Météo-France non-hydrostatic convective-scale atmospheric model AROME (Seity et al. 2011) was run in a dedicated version named AROME-WMED (Fourrié et al. 2015), producing each day 48 hours of forecast from 00UTC. A complete evaluation of the air-sea conditions in the AROME-WMED forecasts during SOP1 was done in a previous study (Rainaud et al. 2016). It showed that AROME-WMED forecasts fit very well with the meteorological observations over sea. However, significant biases (up to 4°C for the 2 m-temperature) were found very locally in the Gulf of Lion during a severe mistral/tramontane wind event (28 October 2012). Two possible sources of errors were identified: i) an overestimation of the sensible heat flux for such conditions by the turbulent fluxes bulk parameterization and ii) the fact that the SST does not evolve during the 48h-forecast, remaining as the initial analysis. This paper aims to address this latter issue by evaluating the impact of an evolving SST during the forecast, through a high-resolution 3D ocean-atmosphere coupling with the AROME-NEMO WMED system, on the representation of the air-sea interface processes and of two HPEs that occurred during SOP1.

The paper is organized as follows. The section 2 presents the numerical ocean-atmosphere coupled system and the experiments. The section 3 describes the two case studies. The impact of the coupling on the air-sea interface is shown in section 4, then in section 5, we describe the impact on the intense meteorological event forecast. Finally, the conclusions and perspectives of this work are given in the section 6.

## 2. Models and experiments

### 2.1. The AROME-NEMO WMED coupled system

The coupled system AROME-NEMO WMED combines the AROME atmospheric model (Seity et al. 2011) and the NEMO ocean model (Madec et al. 2008). The coupling interface includes SURFEX (Masson et al. 2013) and OASIS3-MCT (Valcke 2013).

158 2.1.1. *The atmospheric model* 196 2.1.2. *The ocean model*

159 The atmospheric model, AROME-WMED (Fourrié et al. 2015) 198  
160 is the HyMeX dedicated version of AROME. It ran in real-time 199  
161 during the HyMeX SOP1 field campaign, producing each day a 200  
162 48-hour forecast from the 00UTC AROME analysis. AROME- 201  
163 WMED covers a large domain over the Western Mediterranean 202  
164 area, from Portugal to Sicily and from the Atlas mountains 203  
165 to Northern Alps (Fig. 2). This model is non-hydrostatic and 204  
166 has a 2.5 km-horizontal resolution with 60 stretched  $\eta$ -vertical 205  
167 levels extending from near the surface (almost 10 m) to the 206  
168 top of the troposphere (around 1 hPa). The advection scheme is 207  
169 semi-lagrangian and the temporal scheme is semi-implicit. The 208  
170 boundary conditions are provided by the hourly forecast from 209  
171 the Météo-France global model, ARPEGE (Action de Recherche 210  
172 Petite Echelle Grande Echelle, Courtier et al. 1991). The turbulent 211  
173 scheme is the Cuxart et al. (2000) 1.5 TKE scheme used only 212  
174 for the vertical turbulence. Because AROME is a non-hydrostatic 213  
175 model and thanks to its horizontal resolution, the deep convection 214  
176 is explicitly solved, while the shallow convection is parameterized 215  
177 with EDKF (Eddy Diffusion Kain Fritsch, Kain and Fritsch 1990). 216  
178 The evolution of the five hydrometeor species (rain, snow, graupel, 217  
179 cloud ice and cloud liquid vapor) is given by the ICE3 scheme 218  
180 (Pinty and Jabouille 1998). The surface scheme in AROME- 219  
181 WMED is SURFEX (Masson et al. 2013). Each grid mesh is 220  
182 split into four tiles: land, towns, sea, and inland waters (lakes 221  
183 and rivers). Output fluxes are weight averaged inside each grid 222  
184 box according to the fraction of each respective tile, before being  
185 provided to the atmospheric model. The Interactions between Soil,  
186 Biosphere, and Atmosphere (ISBA) parameterization (Noilhan  
187 and Planton 1989) is activated over land tiles, whereas the  
188 Town Energy Budget (TEB) scheme is used for urban tiles  
189 (Masson 2000). Concerning inland waters, the Charnock (1955)'s  
190 formulation is used. Based on Rainaud et al. (2016)'s results, the  
191 sea surface turbulent fluxes bulk parameterization used is COARE  
192 3.0 (Fairall et al. 2003) in this study. Radiative fluxes are computed  
193 with the Fouquart and Bonnel (1980) scheme (shortwave) and  
194 RRTM (Rapid Radiative Transfer Model, Mlawer et al. 1997)  
195 scheme (longwave).

The ocean model, NEMO-WMED36 (Lebeaupin Brossier et al. 2014), is a regional version of NEMO over the Western Mediterranean Sea (Fig. 2) with a horizontal resolution of  $1/36^\circ$  over an ORCA grid and with 50 z-stretched vertical levels with a 1-m thick first level. The domain has two open boundaries: one west at  $4.8^\circ\text{W}$  (60 km east of Gibraltar Strait) and one south at  $37^\circ\text{N}$  across the Sicily Channel. The Strait of Messina between Sicily and continental Italy is closed. The open boundary conditions come from the PSY2V4R4 daily analyses of Mercator-Océan, smoothed with a monthly averaging to avoid abrupt incoming flows. The PSY2 operational system (Lellouche et al. 2013) has a  $1/12^\circ$  horizontal resolution and covers the North-Eastern Atlantic Ocean, the North and Baltic Seas and the Mediterranean Sea.

In NEMO-WMED36, the tracer advection is computed using a TVD scheme (Barnier et al. 2006) to conserve energy and enstrophy. The turbulence closure scheme is the Blanke and Delecluse (1993) 1.5 TKE scheme, and in case of instabilities, the diffusivity coefficient is fixed at  $10\text{ m}^2\text{ s}^{-1}$  (Lazar et al. 1999) to parameterize ocean deep convection. The sea surface height (SSH) is given by the filtered free surface scheme of Roulet and Madec (2000) and permits to keep a sea volume constant. The bottom friction follows a quadratic function with a coefficient which depends on the 2D mean tidal energy (Lyard et al. 2006). The runoffs are applied on the surface of the river mouths and come from the Beuvier et al. (2010) climatology.

2.1.3. *The air-sea coupling interface*

The coupled system AROME-NEMO is implemented using the SURFEX-OASIS coupling interface (Voldoire et al. 2017). This interface permits the field exchanges between the atmospheric and ocean models (Fig. 2). NEMO provides to OASIS the mean SST and horizontal surface current components ( $u_s$  and  $v_s$ ) at the coupling frequency of one hour. These fields, after interpolation onto the AROME (SURFEX) grid, are used to compute surface fluxes at each subsequent atmospheric time step. The air-sea fluxes at the interface - namely the solar heat flux  $Q_{sol}$ , the net heat flux  $Q_{net}$ , the two components of the horizontal wind stress  $\tau_u$  and

234  $\tau_v$  and the atmospheric freshwater flux  $EMP$  - are computed by  
235 SURFEX and provided to OASIS, which then averages them over  
236 one hour, interpolates and sends them to NEMO at the coupling  
237 frequency.

238 The air-sea fluxes are computed taking into account near  
239 surface atmospheric and oceanic parameters, following the  
240 radiative schemes and turbulent fluxes parameterization:

$$Q_{sol} = (1 - \alpha)SW_{down} \quad (1)$$

$$Q_{net} = Q_{sol} + LW_{down} - \epsilon\sigma SST^4 - H - LE \quad (2)$$

242 where  $SW_{down}$  and  $LW_{down}$  are the incoming components of  
243 the solar and infrared radiations, respectively.  $\alpha$  is the albedo,  $\epsilon$  is  
244 the emissivity and  $\sigma$  is the Stefan-Boltzman constant. Turbulent  
245 heat fluxes ( $H$  for sensible and  $LE$  for latent) are calculated with  
246 the COARE 3.0 parameterization (as suggested by Rainaud et  
247 al. (2016)'s results) and depend on the wind speed and on the  
248 air-sea gradients of temperature and humidity, respectively. The  
249 atmospheric freshwater flux is given by:

$$EMP = E - P_l - P_s \quad (3)$$

250 where  $E$  is the evaporation, corresponding to  $E = LE/\mathcal{L}_v$  with  
251  $\mathcal{L}_v$  the vaporization heat constant.  $P_l$  and  $P_s$  are the liquid and  
252 solid surface precipitation rates (given by AROME-WMED).

253 The wind stress takes into account the ocean surface current  
254 (given by NEMO-WMED36):

$$\vec{\tau} = (\tau_u, \tau_v) = \rho_a C_D (U_s - U_a)(\vec{U}_s - \vec{U}_a) \quad (4)$$

255 with  $\rho_a$  the air density,  $C_D$  the drag coefficient given by the  
256 turbulent fluxes parameterization,  $\vec{U}_a = (u_a, v_a)$  the wind at the  
257 lowest atmospheric model level (almost 10 m here) and  $\vec{U}_s =$   
258  $(u_s, v_s)$  the ocean surface current.

259 The AROME-WMED domain is more extended than the  
260 NEMO-WMED36 domain west of the Gibraltar Strait and south  
261 of the Sicily Channel (Fig. 2). In addition, the Atlantic Ocean and  
262 the Adriatic Sea are not represented in NEMO-WMED36. So, in  
263 these areas, there is no air-sea coupling: the SST comes from the

AROME-WMED initial analysis and is constant during the run,  
and, horizontal current is considered null.

## 2.2. Sensitivity experiments

To evaluate the impact of the air-sea coupling on the forecast  
of severe weather events, three sensitivity experiments have been  
performed for two case studies (see section 3).

The reference experiment (called ARCO) is an atmosphere-  
only AROME-WMED experiment. In ARCO, the initial  
conditions come from the AROME-WMED analysis, in particular  
the analysed SST, which is built by combining a 2D optimal  
interpolation of in-situ data with the CANARI system (Taillefer  
2002) and the OSTIA (Donlon et al. 2012) product (see Rainaud et  
al. 2016, for more details on the AROME-WMED SST analysis).  
In ARCO, the SST field is kept constant during the forecast cycle.

The CPLOA experiment is the ocean-atmosphere coupled  
run using AROME-NEMO WMED. The atmospheric initial  
conditions come from the AROME-WMED analysis. For every  
4-day case study, 48-hour forecasts are issued each day from  
the 00UTC analysis. The first day, the ocean is initialized from  
the outputs of a free (without any data assimilation) NEMO-  
WMED36 simulation (Rainaud 2015). This free ocean simulation  
was itself initialized on 5 September 2012 (at the beginning  
of HyMeX SOP1) by the Mercator Océan PSY2V4R4 analysis  
and driven by air-sea fluxes obtained from the AROME-WMED  
forecasts (Rainaud et al. 2016). For the following forecast  
production cycles, the ocean conditions at 00UTC (day D) are  
provided by the CPLOA 24-hour [ocean] forecast based on the day  
before (D-1; range +24h). The scheme in Figure 3 summarizes the  
protocol of the CPLOA experiment. From an atmospheric point-  
of-view, CPLOA is similar to ARCO except the initial SST field  
and that the SST evolves interactively during the forecast.

The third experiment (called SSTR) is also an atmosphere-  
only AROME-WMED experiment, but it uses the SST issued  
from CPLOA at 00UTC each day and keeps it constant during the  
48h-forecast. This experiment permits to distinguish the impact of  
the modification of the initial SST field (ARCO versus SSTR)  
from the impact of the interactive SST evolution allowed by  
the coupling (SSTR versus CPLOA). As the ocean initial state  
is taken from a free-running ocean simulations without data



1 303 assimilation of oceanic observations in CPLOA and SSTHR, (2016) and Rainaud et al. (2016). The MCS that formed over 341  
2 304 the SST field of these experiments are expected to have greater South-Eastern France was fed by a marine moist southwesterly 342  
3 305 biases with respect to the observations than the AROME analysis low-level jet topped with a drier layer and extremely dry air 343  
4 306 used in ARCO, but with finer and more realistic patterns. above 2500m ASL. The first convective cells developed around 344  
5 307 While some comparisons against observations are provided in the midday on 14 October 2012 over the first foothills facing the 345  
6 308 following, their objective is mainly to support the evaluation of moist and conditionally unstable low-level flow advected from 346  
7 309 the differences between the simulations rather than as an objective the Sea. According to Duffourg et al. (2017, rev) using a realistic 347  
8 310 measure of the benefit of ocean-atmosphere coupling for high- 2.5km-resolution simulation, downstream of the upward motions, 348  
9 311 resolution NWP systems (in which data assimilation should be evaporative cooling under the precipitating cells appeared. This 349  
10 312 used to produce the initial ocean state). initiated a backbuilding process with new convective cells forming 350  
11  
12  
13  
14  
15  
16

### 17 313 3. Case studies

18  
19  
20 314 Two case studies have been chosen from the HyMeX SOP1 period by evaporative cooling under the precipitating cells progressively 353  
21 315 because they include the two kinds of intense weather events of filled the valleys and then spread out over the plains upstream of 354  
22 316 interest: first a moderate mistral episode followed by an HPE the coastal orography, blocking the inland advection of the marine 355  
23 317 during the Intense Observation Period 13 (IOP13, Rainaud et moist low-level flow. After 15UTC, the main convective ascents 356  
24 318 al. (2016)), and secondly, an HPE followed by a severe mistral were located not only on the coastal mountainsides but also on 357  
25 319 event during IOP16a/b (Ducrocq et al. 2014; Duffourg et al. the leading edge of the cold air pool. The cold pool thus played 358  
26 320 2016). Moreover, for these two IOPs, air-sea exchanges have a major role in shifting the location of the precipitation from the 359  
27 321 been suggested playing a significant role (Rainaud et al. 2016; bottom of the valleys to the coasts and over the sea. The most 360  
28 322 Thévenot et al. 2016). A brief description of the events is given in intense convection and heavy precipitation in the French Azur 361  
29 323 the following. Riviera and Italy (Gulf of Genoa) occurred between 14 October 362  
30  
31  
32  
33  
34

#### 35 324 3.1. IOP13: Moderate mistral followed by HPE

36 325 The IOP13 took place between 12 and 15 October 2012. tornado was also observed near Marseille (Ducrocq et al. 2014). 365

37 326 According to Rainaud et al. (2016), the event has been split in For this case, the three experiments start on 11 till 14 October 366  
38 327 three phases following the wind regime. The first phase, from 12 2012. 367

#### 39 328 3.2. IOP16a/b: HPE followed by a severe mistral event 368

40 329 by high surface pressure over Catalonia and low surface pressure The second case study, between 26 and 29 October 2012, is 369  
41 330 over Liguria inducing mistral and tramontane over the Gulf of composed of two IOPs: IOP16a the 26 October and IOP16b the 370  
42 331 Lion. During this first phase, convective precipitation occurred in 27-28 October. 371

43 332 The study of Duffourg et al. (2016) details the mechanisms 372  
44 333 acting during IOP16a. On the early morning of 26 October, moist 373  
45 334 and conditionally unstable air was carried by a south-easterly low- 374  
46 335 level jet over the Gulf of Lion where a MCS formed and then split 375  
47 336 in two separate systems. One of the MCS (MCS1a) progressed 376  
48 337 northwards from 06UTC then decaying over the Cévennes (Massif 377  
49 338 Central). The other one (MCS1b) progressed northeastwards over 378  
50 339 the Mediterranean Sea and reached the southeastern France coasts 379  
51  
52  
53  
54  
55  
56  
57  
58  
59  
60

(Var region) where it induced up to 150 mm in 24h (Fig. 5b), some local floods and 2 casualties in Toulon. The major initiation and maintenance mechanism was the convergence of the south-easterly low-level jet with the south-westerly flow along the Spanish coasts, associated with a secondary low pressure anomaly that formed in the lee of the Iberian mountains, as highlighted by Duffourg et al. (2016). As this surface low progressed eastwards and deepened, the convergence line intensified. Near surface cooling appeared below the MCS that perturbed the low-level flow and intensified the low-level convergence. A third MCS called MCS2 formed on the Gulf of Genoa and affected the Italian coasts, inducing up to 250 mm in 24h (Fig. 5b). In this paper, only the impact on forecast of MCS1a and MCS1b is examined.

The next day, the low reached the Gulf of Genoa, where it stayed till the end of 28 October. Associated with a very cold air break at high levels, it induced a severe mistral from the south of France and the Gulf of Lion to Corsica, Tunisia and the Tyrrhenian Sea. This severe wind event induced 2 fatalities in France. High waves (significant height up to 6.5 m at the LION buoy) were observed from Catalonia, Balearic Islands, France to Italy inducing damages. Finally, this mistral episode produced a drastic change of the whole Western Mediterranean Sea in terms of stratification, with a very rapid and intense cooling and a large mixing, as evidenced by Lebeauin Brossier et al. (2014).

For this case, our sensitivity experiments start on 25 till 28 October 2012.

#### 4. Effects on the air-sea interface

##### 4.1. Sea Surface Temperature

The air-sea coupling impact is first examined on the SST field, after 48h of simulation.

For 13 October 00UTC, the CPLOA and SSTHR SST field present finer scale structures than in ARCO (Fig. 6a,d,g). The ARCO SST is slightly higher ( $\leq 0.5^\circ\text{C}$ ) than the CPLOA SST after 48h forecast, on average over the entire domain. The largest differences are found in the Alboran Sea, the southern Tyrrhenian Sea and around the Balearic Islands (Fig. 6m). Locally, the SST in ARCO is lower, notably in the Gulf of Lion and along the Algerian coasts. These discrepancies come mainly from the different initial

SST field rather than from the SST evolution during the forecast run, as the differences between ARCO and SSTHR (Fig. 6j) are larger than between SSTHR and CPLOA (Fig. 6p). The cooling induced by mistral during the phase 1 of IOP13 and simulated by CPLOA is small (Fig. 6d).

For IOP16a (27 October 00UTC), the SST in ARCO is lower than in CPLOA in the Gulf of Lion but higher in the south of the domain (Fig. 6b,e,n). The SST differences between ARCO and CPLOA arise mainly from the differences in the initial conditions (Fig. 6k,n,q). Indeed, the ocean surface evolution in 48h is small in CPLOA (if compared to SSTHR, Fig. 6e,h,q). Locally, large differences in term of gradient are found between ARCO and CPLOA. For example, between the Gulf of Lion and the Balearic Islands, the SST meridian gradient is  $\sim 1^\circ\text{C}$  in  $\simeq 100$  km in CPLOA while it is around  $3^\circ\text{C}$  in  $\sim 100$  km in ARCO. At the same time, the zonal gradient in the Ligurian Sea is more pronounced in CPLOA than in ARCO.

Looking at the 48h forecast for 29 October 00UTC (IOP16b), the coupled SST is significantly lower than the ARCO SST (almost  $2^\circ\text{C}$  over the basin, Fig. 6c,f,o) while the ARCO and SSTHR SST are relatively similar in terms of mean values (Fig. 6f,i,l). This shows the major evolution of the OML during the two days of IOP16b (Fig. 6r), which is not taken into account in the uncoupled forecast. This strong ocean cooling is more stamped in the Gulf of Lion (Fig. 6r) and is equitably distributed along the two days. It is due to two different mechanisms, as highlighted in Lebeauin Brossier et al. (2014): First, dry and cold air transported by mistral leads to strong air-sea gradient of temperature and humidity at the sea surface, so to strong turbulent fluxes corresponding to extraction of heat and moisture from the OML to the low-level troposphere. Secondly, the strong wind induced a large turbulent mixing in the ocean, so, a deepening of the OML, which entrains colder water from below the ocean thermocline.

To sum-up, the large differences in SST between the uncoupled and coupled runs are due to the presence of fine structures in CPLOA (and SSTHR). Indeed, the NEMO-WMED36 ocean model produces numerous mesoscale eddies and fronts in the Western Mediterranean basin and well reproduces the dynamics and main patterns of the surface circulation described by Millot

(1999), *i.e.* the anticyclonic gyre in the Alboran Sea, the Algerian current and coastal eddies, the Northern Current and the Balearic front. On the contrary, the AROME SST analysis used in ARCO exhibits a smooth north-south gradient. Even though the daily OSTIA SST product is refreshed by the assimilation of 3-hourly observations for the AROME SST analysis, the in-situ data are too few to permit to describe these fine-scale structures. Nevertheless, the AROME-WMED SST analysis (used in ARCO) is updated every day with observations unlike the simulated SST of NEMO-WMED36 (used as initial conditions for SSTHR and evolving in CPLOA). The comparison between SSTHR and CPLOA shows that the interactive coupling may produce very large differences up to 5°C after only 48h due both to large surface forcing and ocean turbulent mixing.

#### 4.2. Turbulent fluxes

The impact of the coupling on turbulent fluxes is evaluated when the strong low-level wind is established over sea for IOP13 phase 3 (14 October 18UT), IOP16a (26 October 12UT) and IOP16b (28 October 00UT). In the following, we consider separately the *short-range* forecast (hereafter SR) as the forecast from +1h to +24h and the *long-range* forecast (hereafter LR) from +25h to +48h. Figure 7 compares the hourly total turbulent heat flux, which is the sum  $-(H + LE)$  and is negative for an ocean [atmospheric] heat loss [gain].

For the two HPE situations, *i.e.* IOP13 phase 3 and IOP16a, the total heat flux is between -50 and -250 W m<sup>-2</sup> in the reference experiment ARCO. Larger [in absolute value] heat losses up to -500 W m<sup>-2</sup> are found near the Balearic Islands, where there is a maximum in the south-westerly low-level wind intensity (Fig. 7). For IOP13, another maximum of heat loss (-500 W m<sup>-2</sup>) is found near the coasts of the Gulf of Lion associated with a new onset of a mistral spell. Considering SR, in CPLOA and SSTHR, the heat loss is slightly lower (by only ~4 W m<sup>-2</sup> on average) than in ARCO (Fig. 7). The SST fine scale structures in CPLOA and SSTHR induce local differences in the temperature and humidity air-sea gradients which lead to significant local differences in the flux fields ( $\pm 200$  W m<sup>-2</sup>) with respect to ARCO ones, in particular near the Balearic Islands and in the Gulf of Lion, where the wind is the most intense. The simulated ocean

evolution is small during these two HPEs. As a consequence the flux differences are small between CPLOA and SSTHR (for SR and LR, not shown). The differences between CPLOA-LR and CPLOA-SR (not shown) are similar to the differences between ARCO-LR and ARCO-SR, *i.e.* mostly due to differences in the atmospheric forecast.

For IOP16b, corresponding to the strong mistral spell, the total turbulent heat loss affects a wide part of the Western Mediterranean Sea and is very high [in absolute value], up to -1500 W m<sup>-2</sup> in the Gulf of Lion (Fig. 7). For SR forecasts, the heat loss in CPLOA is globally lower (by 20 W m<sup>-2</sup>) than in ARCO. Even if there are turbulent flux differences due to initial SST conditions as estimated by comparing ARCO to SSTHR, there is a significant part (50% on average) of the differences between CPLOA and ARCO which is due to the ocean evolution. Indeed, the ocean cooling due to mistral reduces the air-sea temperature gradient, itself inducing a decreasing of the heat loss. The impact of the interactive ocean is more significant (difference up to 500 W m<sup>-2</sup>) for LR forecasts because of a longer drift from the ocean initial state corresponding to the large cooling of 5°C in 48h in the Gulf of Lion in that case (as shown in Fig. 6f,i).

## 5. Impacts on intense weather event forecast

### 5.1. Heavy precipitation

The impact of the air-sea coupling is investigated here for heavy precipitation during the IOP13 phase 3 and IOP16a. In the following, if the ARCO experiment serves as a reference, as it is the state-of-the-art of the current high-resolution NWP system, the role of the air-sea coupling on the forecast is only shown when comparing CPLOA with SSTHR.

#### 5.1.1. Rainfall amounts

For all the SR experiments of IOP13 phase 3, the location of precipitation over South-Eastern France is overall in agreement with rain-gauge observations (Figs. 5a and 8), even if, the heaviest precipitation in ARCO-SR experiment occur around Nice whereas it is more extended from Nice to Genoa in CPLOA-SR and SSTHR-SR experiments (Fig. 8). BIAS, RMSE and correlation coefficients have been computed for the 24-h accumulated rainfall

1 534 amounts for the three simulations against observations (Tab. 1).  
 2  
 3 535 In addition, categorical scores considering different thresholds of  
 4  
 5 536 daily accumulated rainfall amount were also computed (see the  
 6  
 7 537 Appendix for definition). Figure 9 shows the POD, FBIAS and  
 8  
 9 538 ETS scores. These scores show globally that ARCO is closer  
 10  
 11 539 to the observations than SSTHR. The discrepancies between the  
 12  
 13 540 experiments appear only for higher thresholds (< 10 mm in  
 14  
 15 541 24 h). A SST evolving during the forecast run improves the  
 16  
 17 542 scores (CPLOA to compare to SSTHR). For the LR experiments,  
 18  
 19 543 the precipitating system is located further inland, in comparison  
 20  
 21 544 with observations. The scores against rain-gauge data confirm  
 22  
 23 545 weaker performances of the longer range experiments than the  
 24  
 25 546 shorter range ones (Tab. 1 and Fig. 9). In addition, the differences  
 26  
 27 547 between the LR experiments are weaker, even though ARCO is  
 28  
 29 548 still the closest to the observations. No difference is clearly found  
 30  
 31 549 in the mesoscale environment and the mechanisms involved in  
 32  
 33 550 heavy precipitation during IOP13 (see Fig. S1 in the supporting  
 34  
 35 551 information file). The differences in precipitation seem rather due  
 36  
 37 552 to small differences in the moisture contribution of the Western  
 38  
 39 553 Mediterranean Sea throughout the simulation integration, which  
 40  
 41 554 slightly modify the instability of the marine low-level flow. This  
 42  
 43 555 point is examined with water budgets in the following section.

35 556 For the IOP16a, all the SR forecasts simulate rainfall amounts  
 36  
 37 557 over the Cévennes linked to MCS1a larger than observed (Figs. 5b  
 38  
 39 558 and 10). The simulations show more differences between them for  
 40  
 41 559 MCS1b, with the best representation of rainfall amounts over the  
 42  
 43 560 Var region for CPLOA-SR (Figs. 5b and 10). The scores against  
 44  
 45 561 the 24h-cumulated rainfall observations indicate overall weak  
 46  
 47 562 performances for the three experiments (Tab. 2, Fig. 11). This is  
 48  
 49 563 also the case for the LR experiments. Any experiment performs  
 50  
 51 564 better than the others as the ranking varies from one score to an  
 52  
 53 565 other. Larger differences between experiments are found for the  
 54  
 55 566 LR forecasts (Fig. 10) when comparing the heavy precipitation  
 56  
 57 567 associated with MCS1a and MCS1b. CPLOA-LR underestimates  
 58  
 59 568 intense rainfall associated with MCS1b and represents too intense  
 60  
 569 rainfall for MCS1a. On the contrary, ARCO-LR simulates a more  
 570  
 571 570 intense MCS1b. Finally, SSTHR-LR is between the two other  
 572  
 573 571 experiments and represents intense rainfall for the two MCS.

572 The mechanisms involved in the formation and evolution  
 573 of MCSs (Duffourg et al. 2016) are the same for the three

574 experiments. Locally differences in the mesoscale environment 574  
 575 simulated by the three SR or LR experiments are perceptible (see 575  
 576 Fig. S2 and S3 in the supporting information file). As example, 576  
 577 for LR forecasts, instability and moisture are lower in the south- 577  
 578 westerly low-level flow (around the Balearic Islands) in CPLOA- 578  
 579 LR and SSTHR-LR compared to ARCO-LR. This can be related 579  
 580 to a lower SST and to lower heat fluxes in this area. However, as 580  
 581 the largest contributing area of moisture is located in the south- 581  
 582 easterly flow (West of Sardinia), these differences lead to small 582  
 583 impacts on the convection intensity. The secondary surface low 583  
 584 which forms in the lee of the Pyrenees deepens more in SSTHR- 584  
 585 LR than in CPLOA-LR, itself more than in ARCO-LR. The air 585  
 586 cooling in the same area is also less intense in SSTHR-LR than 586  
 587 in CPLOA-LR, itself less than in ARCO-LR. Indeed, the SST and 587  
 588 the heat fluxes are lower in this area in ARCO-LR than in CPLOA- 588  
 589 LR/SSTHR-LR at the beginning of the simulation. During the 589  
 590 CPLOA simulation, SST progressively slightly decreases, and so 590  
 591 do the surface heat fluxes in absolute value. These differences 591  
 592 in terms of surface heat fluxes directly affect the low-level 592  
 593 atmosphere stability and then the cyclonic circulation at low- 593  
 594 level and thus it slightly modifies the convergence in the Gulf of 594  
 595 Lion and the convection organization. CPLOA-LR underestimates 595  
 596 intense rainfall associated with MCS1b and represents too intense 596  
 597 rainfall for MCS1a. On the contrary, ARCO-LR simulates a more 597  
 598 intense MCS1b. Finally, SSTHR-LR is between the two other 598  
 599 experiments and represents intense rainfall for the two MCSs. 599

### 5.1.2. Water budgets 600

601 In order to analyze how much the water vapour amount within 601  
 602 the atmospheric boundary layer is different, and thus the water 602  
 603 supply available for heavy precipitation systems, total water 603  
 604 content budgets are computed over a 3D box over the North- 604  
 605 Western Mediterranean. The water budget computation follows 605  
 606 Duffourg and Ducrocq (2013), with the time variation of the total 606  
 607 atmospheric water (vapour and hydrometeors) storage  $S$  given by: 607

$$\Delta S = E - P + (Q_n + Q_e + Q_s + Q_w) + r \quad (5)$$

608 where  $E$  is surface evaporation and  $P$  precipitation in surface 608  
 609 (corresponding to atmospheric water losses for the box).  $Q_n$ ,  $Q_e$ , 609

610  $Q_s$  and  $Q_w$  are the vertically integrated horizontal water fluxes  
611 across the vertical sides of the box for the north, east, south and  
612 west faces, respectively.  $r$  is the sum of the vertical transport at the  
613 top of the box and of a residual term due to the offline computation  
614 of the different terms.  $r$  has been verified as negligible when the  
615 top of the box is the model highest layer, so, for a less thick layer,  
616  $r$  is controlled by the vertical flow at the top of the box.

617 The water budget is evaluated for a 50 hPa-height (correspond-  
618 ing to nearly 500 m) box covering a wide part of the North-  
619 Western Mediterranean Sea (Fig. 12) in order to focus on the  
620 marine low-level flow feeding the convective systems. Figure 13a  
621 presents the budget terms during IOP13 phase 3 in CPLOA. The  
622 vertically integrated horizontal water fluxes reflect the low-level  
623 atmospheric circulation which mainly consists of a southerly to  
624 southeasterly flow, with thus water inputs from the south, then  
625 from the south-west, and outputs to the north and east. Precipita-  
626 tion is simulated in the evening (after 18UTC) in the box, thus  
627 corresponding to a water loss (Fig. 13a). As precipitation starts,  
628  $r$  becomes larger in absolute value, with negative values between  
629 16UT and 21UT related notably to an upward flux of water due to  
630 convection, then positive indicating a water gain, *i.e.* a downward  
631 flux on average through the top of the box. Evaporation from sea  
632 increases along the day from 45 to 80  $\text{mg m}^{-2} \text{s}^{-1}$ , due to the  
633 enhancement of the low-level wind during the day.  $E$  represents a  
634 significant contribution to the total water supply, up to 40% of the  
635 water supply (Fig. 13a), mostly from the region between Catalonia  
636 and the Balearic Islands (Fig. 7). But, above all, the largest  
637 contribution comes from outside (south) of the box, possibly from  
638 the Algerian basin as suggested by Rainaud et al. (2016), and  
639 crosses the North-Western Mediterranean area to supply moisture  
640 to the precipitating system over South-Eastern France. Figure  
641 13b allows to assess the impact of coupling on the evaporation  
642 from the Sea. It shows the surface evaporation  $E$  for the three  
643 experiments and for SR and LR forecasts.  $E$  is lower in CPLOA  
644 compared to ARCO, in agreement with the results found in section  
645 4.2 and shown in Figure 7.  $E$  for SSTHR-SR and CPLOA-  
646 SR are close, whereas SSTHR-LR is intermediate in term of  
647 evaporation between ARCO-LR and CPLOA-LR (corresponding  
648 to -10% and +10% for  $E$ , respectively). In conclusion, for that  
649 case, the water budget shows a quite large effect of coupling on

the surface evaporation. The relative impacts of the interactive  
ocean during the forecast run and of the different initial SST  
have been estimated for SR[LR] forecasts to be of about 25[50]%  
and 75[50]%, respectively. For IOP16a, the relative impacts are  
assessed to be 10[20]% for the interactive ocean and 80[90]% for  
the initial SST field (*see Fig. S4 in the supporting information*  
*file*).

## 5.2. Severe mistral

Figure 14 shows the evolution of the wind speed, the 2 m-  
temperature and the SST at the LION buoy [ $4.7^\circ\text{E}$ - $42.1^\circ\text{N}$ ] during  
IOP16b (27-28 October 2012). It shows the large increase in  
the wind speed and the decrease in temperature associated with  
the mistral. All the experiments reproduce quite well this rapid  
evolution of the low-level atmosphere. At the end of 28 October  
(range +42 to +46h), as the wind starts decreasing, differences  
between the experiments are maximum. The 10 m-wind speed  
is lower by  $0.8 \text{ m s}^{-1}$  in SSTHR and by  $1.5 \text{ m s}^{-1}$  in CPLOA  
compared to ARCO. However, compared to the buoy observation,  
all the experiments overestimate the wind speed (by up to  $5 \text{ m s}^{-1}$   
at range +30h). The largest differences in the 2 m-temperature  
between the experiments are also found on 28 October: up to  
 $+0.1^\circ\text{C}$  for SSTHR and of  $-0.4^\circ\text{C}$  for CPLOA compared to  
ARCO. In the coupled run, the cold front induced by the mistral  
goes a little more to the south than in ARCO (not shown).  
This is probably due to a cooler atmospheric boundary layer  
as an integrated effect of the lower SST and heat fluxes under  
mistral (Fig. 6c,f,i and 7) and also to the triggering of the frontal  
convection more in the south related to the position of the warm  
Algerian eddies in CPLOA (Fig. 6f).

As already highlighted, during this mistral event, the SST  
strongly decreases (Fig. 14). This decrease is only represented  
in the coupled experiment ( $-2.3^\circ\text{C}$  in 48h against  $-4^\circ\text{C}$  in 48h  
observed at the LION buoy). However, CPLOA presents initial  
and final biases in SST. In the morning of 27 October, the cold  
SST bias ( $-0.8^\circ\text{C}$ ) is associated with a too thin OML (20 m-  
depth against 30 m-depth according to temperature observation  
from the bathymetric thermistance chain at the LION buoy). This  
is due to errors in the initial ocean state issued from the free  
NEMO-WMED36 run started at the beginning of September and

not refreshed by ocean data assimilation since then. The biases in SST and thermocline position at Lion are indeed already present before IOP13 and IOP16a (see Fig. S5 and S6 in the supporting information file). On the afternoon of 28 October, CPLOA SST is overestimated (+0.9°C) although the Mixed Layer Depth (MLD) is around 50 m-depth as observed. In fact, this overestimation is explained by too warm waters located below the OML which make the cooling by entrainment at the bottom of OML not intense enough in CPLOA.

As also shown by Lebeauvin Brossier et al. (2014), the OML cooled and deepened drastically over the whole Western Mediterranean basin during IOP16b due to large surface heat loss and turbulent mixing. The coupled experiment presented here shows the important role of the OML during this severe mistral event with at the same time a downward heat transport below the thermocline to the deeper ocean layers by mixing/deepening, and, in surface a moderation of the sensible and latent heat fluxes in absolute value and of the evaporation. As a consequence, the 2m-air temperature (and 2m-specific humidity, not shown) is slightly lower in the CPLOA forecast (than in SSTHR, Fig. 14).

## 6. Conclusions and perspectives

This study presents the first application and validation of the high-resolution high-frequency air-sea coupled model AROME-NEMO WMED, considering the most frequent severe weather events of the Western Mediterranean region, *i.e.* HPEs and mistral. Using three sensitivity experiments, the impact of two different effects on the atmospheric forecast were considered: the change in the initial SST field and the impact of an interactive 3D ocean. This study aims at investigating the role of the air-sea coupling on the forecast with the comparison between CPLOA and SSTHR. If ARCO serves as a reference, it is important to point out that the coupled experiment design, with the use of free-running simulation to initialize the ocean model, prevents from a direct verification of the forecast skill.

For IOP13, corresponding to a moderate mistral episode followed by an HPE, the coupled interactive ocean induces a small decrease in the SST and in the surface heat fluxes. Nevertheless, the location of the heaviest precipitation is modified. An analysis of the water budget highlights that, despite a weak OML evolution

during that case, coupling leads to a decrease in the Mediterranean Sea evaporation and water supply by up to ~20% compared to the ARCO experiment, but more than a half is due to the change in the initial SST field. In addition, the two moisture extracting areas (*i.e.* the Catalanian Sea and the Algerian basin) suggested by Rainaud et al. (2016) were confirmed by this budget evaluation.

For IOP16a, a large sensitivity of the MCSs forecast was highlighted. In particular, the intensity of MCS1b over the Var region is completely modified with different sea surface conditions, for the benefit of MCS1a, which affects the Cévennes. In fact, the split of MCS1a in two MCSs which occurred over the Gulf of Lion seems to be very sensitive to the sea surface conditions and, furthermore, the MCS splitting there is a challenging process to correctly reproduce in numerical simulations of IOP16a. As for IOP13, the impact of the interactive ocean evolution is more important for long-range than for short-range forecast, because the OML cooling increases with the forecast range and modifies the intensity of the precipitating system.

The coupled experiment is able represent the intense and rapid OML cooling and deepening which occurred during the severe mistral event of IOP16b. It also confirms Lebeauvin Brossier et al. (2014) results, meaning that, in addition to the large surface heat loss, the entrainment of cold water at the OML base is an efficient process that significantly contributes to the sea surface cooling and, so, that is important to take into account. The OML deepening by entrainment which strongly contributes to the OML cooling by a downward heat transfer into the deeper oceanic layers and thus to the decrease in the surface turbulent heat fluxes towards the atmosphere, is thus a crucial coupled process. AROME-NEMO WMED was also recently applied for the study of dense water formation triggered by mistral and tramontane winds during HyMeX SOP2 (Lebeauvin Brossier et al. 2017), illustrating its benefit for the analysis of the fine-scale air-sea coupled processes.

Finally, the AROME-NEMO coupled system demonstrates that the air-sea interactive coupling affects the high-resolution atmospheric deterministic forecast. Nevertheless, additional sensitivity tests should be performed in order to better estimate the benefit of a ocean-atmosphere coupled systems for operational

1 768 purpose. First, the obtained results only concern two HPEs  
2 769 and one mistral case. Further investigations must be undertaken  
3 770 for several other situations in order to assess the coupling  
4 771 impact. Secondly and as previously mentioned, in our coupled  
5 772 experiments, the ocean initial state arose from a free-running  
6 773 ocean simulation. The ocean state used as initial conditions is  
7 774 thus not as close from the real ocean state as the one that  
8 775 could be obtained through ocean data assimilation of the recent  
9 776 observations. The next step will be thus to use a high-resolution  
10 777 operational ocean analysis to initialize the ocean component  
11 778 of AROME-NEMO coupled system, as those provided by the  
12 779 *Copernicus Marine Environment Monitoring Service (CMEMS)*.  
13 780 The step further towards operational real-time forecast would be  
14 781 to explore strategies for combining ocean data assimilation and  
15 782 atmosphere data assimilation for the AROME-NEMO system.  
16 783 Another perspective is to take into account the sea state with  
17 784 the introduction of a wave model in the coupled system, as it  
18 785 strongly impacts the sea surface turbulent fluxes and thus it can  
19 786 significantly modify the weather forecast (Renault et al. 2012;  
20 787 Ricchi et al. 2016; Thévenot et al. 2016; Bouin et al. 2017 rev.;  
21 788 Voldoire et al. 2017).

### 789 Acknowledgements

790 This work is a contribution to the HyMeX program (*Hydrological*  
791 *cycle in the Mediterranean Experiment - [www.hymex.org](http://www.hymex.org)*)  
792 through INSU-MISTRALS support. The authors acknowledge  
793 the DGA (Direction Générale de l'Armement), a part of the  
794 French Ministry of Defense, for its contribution to Romain  
795 Rainaud's PhD. The authors thank Marie-Noëlle Bouin (CNRM)  
796 and the CMM team of Météo-France who manage and provide  
797 the observations of the LION moored buoy, Mercator Océan  
798 for supplying the PSY2V4R4 analysis and the HyMeX database  
799 teams (ESPRI/IPSL and SEDOO/OMP) for their help in accessing  
800 the data. The authors also thank Nadia Fourrié (CNRM) and  
801 the SWAPP system team (Météo-France) who helped us in the  
802 implementation of the AROME-WMED experiments and coupled  
803 simulations. Finally, the authors gratefully acknowledge Bertrand  
804 Decharme and Aurore Voldoire (CNRM) for their invaluable help  
805 in the SURFEX-OASIS coupling interface development.

The authors want to dedicate this work to the memory of  
Françoise Taillefer, who devoted much of her work to the  
improvement of the marine surface conditions in the Numerical  
Weather Prediction systems of Météo-France. Her enthusiasm and  
encouragements will be missing.

### Appendix

Similarly to Ducrocq et al. (2002), the following skill scores were  
computed using a  $2 \times 2$  contingency table (Tab. A) considering  
different thresholds of rainfall amounts:

- the frequency bias  $FBIAS = (b + d)/(c + d)$ ;
- the probability of detection  $POD = d/(c + d)$ ;
- the equitable threat score  $ETS = (a - H)/(a + b + c - H)$ ;

with  $H = [(a + b)(a + c)]/(a + b + c + d)$  referring to the  
expected number of correct simulated values below the threshold  
with a random simulation. The FBIAS measures the ability of the  
model to forecast the occurrence of the event over the threshold.  
The POD describes the ability in representing the size of the  
event. The ETS score measures the ability to reproduce the event  
taking into account its location.

A perfect forecast has FBIAS, POD and ETS equal to 1.

### Supporting information

The following supporting information is available as part of the  
manuscript:

**Figure S1.** IOP13, 14 Oct 2012 16UT: [*top panels*] Radar reflectivities  
(colors, in  $\text{mm h}^{-1}$  equivalent), Integrated Water Vapor over  $28 \text{ kg m}^{-2}$   
(grey area), wind at 950hPa (arrows,  $\text{m s}^{-1}$ ) and CAPE over  $750 \text{ J kg}^{-1}$   
(red contour), and, [*bottom panels*]  $\theta'_w$  at 925 hPa (colors, in K), wind  
at 925 hPa (arrows,  $\text{m s}^{-1}$ ) and Mean Sea Level Pressure (hPa, black  
contours), in ARCO-LR, CPLOA-LR and SSTHR-LR.

**Figure S2.** IOP16a, 26 Oct 2012 06UT: [*top panels*] Mean Sea Level  
Pressure (colors, in hPa), Radar reflectivities (green contours at 5, 20, and  
 $100 \text{ mm h}^{-1}$  equivalent) and CAPE over  $1000 \text{ J kg}^{-1}$  (red contour), and,  
[*bottom panels*]  $\theta'_w$  at 925 hPa (color, in K) and wind at 925hPa (arrows,  
 $\text{m.s}^{-1}$ ), in ARCO-LR, CPLOA-LR and SSTHR-LR.

**Figure S3.** IOP16a, 26 Oct 2012 12UT: Radar reflectivities (colors,  
in  $\text{mm h}^{-1}$  equivalent), Integrated Water Vapor over  $32 \text{ kg m}^{-2}$  (grey  
area), wind at 950 hPa (arrows,  $\text{m s}^{-1}$ ) and CAPE over  $1000 \text{ J kg}^{-1}$  (red  
contour) in ARCO-SR, CPLOA-SR and SSTHR-SR.

1 845 **Figure S4.** (a) Water budget components ( $\text{mg m}^{-2} \text{s}^{-1}$ ) in CPLOA for  
 2 846 IOP16a (26 October 2012, forecast basis: 26 October 00UTC) for the low  
 3 847 levels (0 - ~500 m) [see the box in Fig. 10]. (b) Evaporation contribution  
 4 848 ( $\text{mg m}^{-2} \text{s}^{-1}$ ) to water budget for 26 October 2012 in ARCO, CPLOA,  
 5 849 and SSTHR for SR forecast (forecast basis: 26 October 00UTC) and LR  
 6 850 forecast (forecast basis: 25 October 00UTC).

7 851 **Figure S5.** IOP13 phase 3 (14-15 October 2012) at the LION  
 8 852 buoy: [top panels] Time-series of 10m-wind speed (FF10,  $\text{m s}^{-1}$ ), 2m-  
 9 853 temperature (T2M,  $^{\circ}\text{C}$ ) and SST ( $^{\circ}\text{C}$ ) for ARCO (black), CPLOA (red)  
 10 854 and SSTHR (blue) (forecast basis: 14 October 2012 00UT. Observations  
 11 855 are the grey circles. [bottom panel] Time-serie of the ocean temperature  
 12 856 ( $^{\circ}\text{C}$ ) profile simulated by CPLOA. The black line indicates the simulated  
 13 857 MLD from a density criteria. The circles are observations from the  
 14 858 bathymetric thermistance chain.

15 859 **Figure S6.** Same as Figure S5 but for IOP16a (26-27 October 2012)  
 16 860 (forecast basis: 26 October 2012 00UT).



- 861 **References**
- 862 Barnier B., Madec G., Penduff T., Molines J.-M., Treguier A.-M., Le Sommer  
863 J., Beckmann A., Biastoch A., Böning C., Dengg J., Derval C., Durand E.,  
864 Gulev S., Rémy E., Talandier C., Theetten S., Maltrud M.E., McClean J.,  
865 and De Cuevas B., 2006: Impact of partial steps and momentum advection  
866 schemes in a global ocean circulation model at eddy-permitting resolution.  
867 *Ocean Dyn.*, **56** (5-6), 543-567, doi:10.1007/s10236-006-0082-1.
- 868 Barthlott, C., S. Davolio, 2016: Mechanisms initiating heavy precipitation over  
869 Italy during HyMeX Special Observation Period 1: a numerical case study  
870 using mesoscale models. *Quart. J. Roy. Meteorol. Soc.*, **142** (S1), 238-  
871 258, doi:10.1002/qj.2630.
- 872 Beuvier J., Sevault F., Herrmann M., Kontoyiannis H., Ludwig W.,  
873 Rixen M., Stanev E., Béranger K., Somot S., 2010: Modeling the  
874 Mediterranean Sea interannual variability during 1961-2000: focus on  
875 the Eastern Mediterranean Transient. *J. Geophys. Res.*, **115**, C08517,  
876 doi:10.1029/2009JC005950.
- 877 Blanke, B., and P. Delecluse, 1993: Variability of the tropical Atlantic ocean  
878 simulated by a general circulation model with two different mixed layer  
879 physics. *J. Phys. Oceanogr.*, **23**, 1363-1388.
- 880 Bouin, M.-N., J.-L. Redelsperger, C. Lebeaupin Brossier, 2017 (rev.): Processes  
881 leading to deep convection and sensitivity to sea-state representation during  
882 HyMeX IOP8 heavy precipitation event. *Quart. J. Roy. Meteorol. Soc.*
- 883 Bresson, E., Ducrocq V., Nuissier O., Ricard D., De Saint-Aubin C., 2012:  
884 Idealized numerical simulations of quasi-stationary convective systems  
885 over the Northwestern Mediterranean complex terrain. *Quart. J. Roy.*  
886 *Meteorol. Soc.*, **138**, 1751-1763, doi:10.1002/qj.1911.
- 887 Buzzi, A., Tartaglione N., Malguzzi P., 1998: Numerical Simulations of the  
888 1994 Piedmont Flood: Role of Orography and Moist Processes. *Mon. Wea.*  
889 *Rev.*, **126** (9), 2369-2383.
- 890 Charnock, H., 1955: Wind stress over a water surface. *Quart. J. Roy. Meteor.*  
891 *Soc.*, **81**, 639-640.
- 892 Courtier, P., C. Freydl, J.-F. Geleyn, F. Rabier, and M. Rochas, 1991:  
893 The ARPEGE project at Météo-France. *ECMWF workshop on numerical*  
894 *methods in atmospheric modeling*, **2**, 193-231.
- 895 Cuxart, J., P. Bougeault, and J.-L. Redelsberger, 2000: A turbulence scheme  
896 allowing for mesoscale and large-eddy simulations. *Quart. J. Roy. Meteor.*  
897 *Soc.*, **126**, 1-30.
- 898 Davolio, S., Stocchi P., Benetazzo A., Bohm E., Riminucci F., Ravaioli M.,  
899 Li X.-M., Carniel S., 2015: Exceptional Bora outbreak in winter 2012:  
900 Validation and analysis of high-resolution atmospheric model simulations  
901 in the Northern Adriatic area. *Dyn. Atmos. Oc.*, **71**, 1-20.
- 902 Delrieu, G., Nicol J., Yates E., Kirstetter P.-E., Creutin J. D., Anquetin S.,  
903 Obled C., Saulnier G.-M., Ducrocq V., Gaume E., Payrastré O., Andrieu H.,  
904 Ayrat P.-A., Bouvier C., Neppel L., Livet M., Lang M., Parent-du-Châtelet  
905 J., Walpersdorf A., Wobrock W., 2005: The Catastrophic Flash-Flood Event  
906 of 8-9 September 2002 in the Gard Region, France: A First Case Study for  
907 the Cévennes-Vivarais Mediterranean Hydrometeorological Observatory. *J.*  
*Hydrometeorol.*, **6** (1), 34-52, doi:10.1175/JHM-400.1.
- Donlon, C. J., M. Martin, J. Stark, J. Roberts-Jones, E. Fiedler, W. Wimmer,  
2012: The operational sea surface temperature and sea ice analysis (OSTIA)  
system. *Remote Sens. Environ.*, **116**, 140-158.
- Drobinski, P., Ducrocq V., Alpert P., Anagnostou E., Béranger K., Borga  
M., Braud I., Chanzy A., Davolio S., Delrieu G., Estournel C., Filali  
Boubrahmi N., Font J., Grubisic V., Gualdi S., Homar V., Ivancan-Picek  
B., Kottmeier C., Kotroni V., Lagouvardos K., Lionello P., Llasat M. C.,  
Ludwig W., Lutoff C., Mariotti A., Richard E., Romero R., Rotunno R.,  
Roussot O., Ruin I., Somot S., Taupier-Letage I., Tintoré J., Uijlenhoet  
R., Wernli H., 2014: HyMeX, a 10-year multidisciplinary program on the  
Mediterranean water cycle. *Bull. Amer. Meteorol. Soc.*, **95** (7), 1063-1082,  
doi:10.1175/BAMS-D-12-00242.1.
- Ducrocq, V., D. Ricard, J.-P. Lafore, F. Orain, 2002: Storm-scale numerical  
rainfall prediction for five precipitating events over France: On the  
importance of the initial humidity field. *Wea. and Forecast.*, **17**, 1236-1256.
- Ducrocq, V., O. Nuissier, D. Ricard, C. Lebeaupin and T. Thouvenin, 2008:  
A numerical study of three catastrophic precipitating events over Southern  
France. II: Mesoscale triggering and stationarity factors. *Quart. J. R.*  
*Meteorol. Soc.*, **134**, 131-145.
- Ducrocq V., Braud I., Davolio S., Ferretti R., Flamant C., Jansa A., Kalthoff  
N., Richard E., Taupier-Letage I., Ayrat P.A., Belamari S., Berne A., Borga  
M., Boudevillain B., Bock O., Boichard J.-L., Bouin M.-N., Bousquet O.,  
Bouvier C., Chiggato J., Cimini D., Corsmeier U., Coppola L., Cocquerez  
P., Defer E., Delanoë J., Di Girolamo P., Doerenbecher A., Drobinski P.,  
Dufournet Y., Fourrié N., Gourley J. J., Labatut L., Lambert D., Le Coz  
J., Marzano F.S., Molinié G., Montani A., Nord G., Nuret M., Ramage  
K., Rison B., Roussot O., Saïd F., Schwarzenboeck A., Testor P., Van  
Baelen J., Vincendon B., Aran M., Tamayo J., 2014: HyMeX-SOP1, the  
field campaign dedicated to heavy precipitation and flash flooding in the  
Northwestern Mediterranean. *Bull. Amer. Meteorol. Soc.*, **95** (7), 1083-  
1100, doi:10.1175/BAMS-D-12-00244.1.
- Ducrocq, V., S. Davolio, R. Ferretti, C. Flamant, V. Homar Santaner,  
N. Kalthoff, E. Richard, H. Wernli, 2016: Advances in understanding  
and forecasting of heavy precipitation in Mediterranean through the  
HyMeX SOP1 field campaign. *Quart. J. R. Meteorol. Soc.*, **142** (S1), 1-6,  
doi:10.1002/qj.2856.
- Duffourg, F., and V. Ducrocq, 2011: Origin of the moisture feeding the Heavy  
Precipitating systems over Southeastern France. *Nat. Hazards Earth Syst.*  
*Sci.*, **11**, 4, 1163-1178.
- Duffourg, F., and V. Ducrocq, 2013: Assessment of the water supply to  
Mediterranean heavy precipitation: a method based on finely designed  
water budgets. *Atm. Sci. Lett.*, **14**, 133-138, doi:10.1002/asl2.429.
- Duffourg, F., Nuissier O., Ducrocq V., Flamant C., Chazette P., Delanoë  
J., Doerenbecher A., Fourrié N., Di Girolamo P., Lac C., Legain D.,  
Martinet M., Saïd F., Bock O., 2016: Offshore deep convection initiation  
and maintenance during HyMeX IOP16a. *Quart. J. Roy. Meteorol. Soc.*,

1 955 142 (S1), 259-274, doi:1002/qj.2725.

2 956 Duffourg, F., K-O. Lee, V. Ducrocq, C. Flamant, P. Chazette, P. Di Girolamo,

3 2017 (rev): Role of moisture patterns in the backbuilding formation of

4 957 HyMeX IOP13 Heavy Precipitating Systems, *Quart. J. Roy. Meteorol. Soc.*,

5 958 Fairall C., Bradley E., Hare J., Grachev A., Edson J., 2003: Bulk

6 parameterization of air-sea fluxes updates and verification for the coare

7 959 algorithm. *J. Clim.*, **16**, 571-591.

8 960 Fouquart Y., Bonnel B., 1980: Computations of solar heating of the earths

9 961 atmosphere: A new parameterization. *Beitr. Phys. Atmos.*, **53**, 35-62.

10 962 Fourrié, N., E. Bresson, M. Nuret, C. Jany, P. Brousseau, A. Doerenbecher,

11 963 M. Kreitz, O. Nuissier, E. Sevault, H. Bénichou, M. Amodei, and

12 964 F. Poupponneau, 2015: AROME-WMED, a real-time mesoscale model

13 965 designed for HyMeX Special Observation Periods. *Geo. Model. Dev.*, **8**,

14 966 1919-1941, doi:10.5194/gmd-8-1919-2015.

15 967 Gaspar P., Grégoris Y., Lefevre J., 1990: A simple Eddy Kinetic Energy model

16 968 for simulations of the oceanic vertical mixing: Tests at Station Papa and

17 969 long-term upper ocean study site. *J. Geophys. Res.*, **95** (C9), 16179-16193.

18 970 Grifoll, M., J. Navarro, E. Pallares, L. Rafols, M. Espino, A. Palomares,

19 971 2016: Ocean-atmosphere-wave characterisation of a wind jet (Ebro shelf,

20 972 NW Mediterranean Sea). *Nonlin. Processes Geophys.*, **23**, 143-158,

21 973 doi:10.5194/npg-23-143-2016.

22 974 Homar, V., R. Romero, D. J. Stensrud, C. Ramis, and S. Alonso, 2003:

23 975 Numerical diagnosis of a small, quasi-tropical cyclone over the western

24 976 Mediterranean: Dynamical vs. boundary factors. *Q. J. R. Meteorol. Soc.*,

25 977 **129**, 1469-1490.

26 978 Kain J. S., Fritsch J. M., 1990: A one-dimensional entraining/detraining plume

27 979 model and its application in convective parameterization. *J. Atmos. Sci.*, **47**

28 980 (23), 2784-2802.

29 981 Lafore, J-P., Stein J., Asencio N., Bougeault P., Ducrocq V., Duron J.,

30 982 Fischer C., Hreil P., Mascart P., Masson V., Pinty J-P., Redelsperger J-L.,

31 983 Richard E., Vila-Guerau de Arellano, J., 1998: The Meso-NH atmospheric

32 984 simulation system. Part I: Adiabatic formulation and control simulations.

33 985 Scientific objectives and experimental design. *Ann. Geophys.*, **16**, 90-109.

34 986 Lazar A., Madec G., Delecluse P., 1999: The deep interior downwelling,

35 987 the Veronis effect, and mesoscale tracer transport parameterizations in an

36 988 OGCM. *J. Phys. Ocean.*, **29** (11), 2945-2961.

37 989 Lebeaupin C., Ducrocq V., Giordani H., 2006: Sensitivity of torrential rain

38 990 events to the sea surface temperature based on high-resolution numerical

39 991 forecasts. *J. Geophys. Res.*, **111** (D12), 1-19, doi:10.1029/2005JD006541.

40 992 Lebeaupin Brossier, C., V. Ducrocq, and H. Giordani, 2008: Sensitivity of

41 993 three Mediterranean heavy rain events to two different sea surface fluxes

42 994 parameterizations in high-resolution numerical modeling. *J. Geophys. Res.*,

43 995 **113**, D21109, doi:10.1029/2007JD009613.

44 996 Lebeaupin Brossier, C., Ducrocq V., Giordani H., 2009: Two-way

45 997 one-dimensional high-resolution airsea coupled modelling applied to

46 998 Mediterranean heavy rain events. *Quart. J. Roy. Meteorol. Soc.*, **135** (638),

47 999 187-204.

48 1000 Lebeaupin Brossier C., Arsouze T., Béranger K., Bouin M-N., Bresson E., 1002

49 1003 Ducrocq V., Giordani H., Nuret M., Rainaud R., Taupier-Letage I., 2014: 1004

50 1005 Ocean Mixed Layer responses to intense meteorological events during 1006

51 1006 HyMeX-SOP1 from a high-resolution ocean simulation. *Ocean Model.*, **84**, 1007

52 1007 84-103, doi:10.1016/j.ocemod.2014.09.009. 1008

53 1008 Lebeaupin Brossier, C., F. Léger, H. Giordani, J. Beuvier, M-N. Bouin, V. 1009

54 1009 Ducrocq, N. Fourrié, 2017: Dense water formation in the north-western 1010

55 1010 Mediterranean area during HyMeX-SOP2 in 1/36° ocean simulations: 1011

56 1011 Ocean-atmosphere coupling impact. *J. Geophys. Res. Oceans*, **122**, 1012

57 1012 doi:10.1002/2016JC012526. 1013

58 1013 Lellouche, J-M., O. Le Galloudec, M. Drévillon, C. Régnier, E. Greiner, G. 1014

59 1014 Garric, N. Ferry, C. Desportes, C-E. Testut, C. Bricaud, R. Bourdallé- 1015

60 1015 Badie, B. Tranchant, M. Benkiran, Y. Drillet, A. Daudin, C. De Nicola, 1016

1016 2013: Evaluation of global monitoring and forecasting systems at Mercator 1017

1017 Océan. *Ocean Sci.*, **9**, 57-81, doi:10.5194/os-9-57-2013. 1018

1018 Lyard F., Lefevre F., Letellier T., Francis O., 2006: Modelling the global ocean 1019

1019 tides: modern insights from FES2004. *Ocean Dynamics*, **56** (5-6), 394-415. 1020

1020 Madec G., and the NEMO system team, 2008: NEMO ocean engine. *Note du* 1021

1021 *Pole de modélisation, Institut Pierre-Simon Laplace (IPSL), France*, No 27 1022

1022 ISSN No 1288-1619. 1023

1023 Masson, V., 2000: A physically-based scheme for the urban energy budget in 1024

1024 atmospheric models. *Bound.-Layer Meteor.*, **94**, 357-397. 1025

1025 Masson, V., P. Le Moigne, E. Martin, S. Faroux, A. Alias, R. Alkama, S. 1026

1026 Belamari, A. Barbu, A. Boone, F. Bouyssel, P. Brousseau, E. Brun, J-C. 1027

1027 Calvet, D. Carrer, B. Decharme, C. Delire, S. Donier, K. Essaouini, A-L. 1028

1028 Gibelin, H. Giordani, F. Habets, M. Jidane, G. Kerdraon, E. Kourzeneva, 1029

1029 M. Lafaysse, S. Lafont, C. Lebeaupin Brossier, A. Lemonsu, J-F. Mafhouf, 1030

1030 P. Marguinaud, M. Mokhtari, S. Morin, G. Pigeon, R. Salgado, Y. Seity, F. 1031

1031 Taillefer, G. Tanguy, P. Tulet, B. Vincendon, V. Vionnet, and A. Voldoire, 1032

1032 2013: The SURFEXv7.2 land and ocean surface platform for coupled or 1033

1033 offline simulation of earth surface variables and fluxes. *Geosci. Model Dev.*, 1034

1034 **6**, 929-960, doi:10.5194/gmd-6-929-2013. 1035

1035 Miglietta, M. M., A. Moscatello, D. Conte, G. Mannarini, G. Lacorata, R. 1036

1036 Rotunno, 2011: Numerical analysis of a Mediterranean 'hurricane' over 1037

1037 south-eastern Italy: Sensitivity experiments to sea surface temperature. 1038

1038 *Atmos. Res.*, **101**, 412-426, doi:10.1016/j.atmosres.2011.04.006. 1039

1039 Millot, C., 1999: Circulation in the Western Mediterranean Sea. *J. Mar. Syst.*, 1040

1040 **20** (1-4), 423-442. 1041

1041 Mlawer, E.J., S.J. Taubman, P.D. Brown, M.J. Iacono and S.A. Clough, 1997: 1042

1042 Radiative transfer for inhomogeneous atmospheres: RRTM, a validated 1043

1043 correlated-k model for the longwave. *J. Geophys. Res.*, **102**, 16663-16682. 1044

1044 Noilhan, J., and S. Planton, 1989: Simple parameterization of land surface 1045

1045 processes for meteorological models. *Mon. Wea. Rev.*, **117**, 536-549. 1046

1046 Nuissier, O., V. Ducrocq, D. Ricard, C. Lebeaupin, S. Anquetin, 2008: A 1047

1047 numerical study of three catastrophic precipitating events over southern 1048

1048 France. I: Numerical framework and synoptic ingredients. *Quart. J. R. 1049*

1049 *Meteorol. Soc.*, **134**, 111-130. 1050

- 1 1049 Nuissier, O., Joly B., Joly A., Ducrocq V., Arbogast P., 2011: A statistical 1096  
2 1050 downscaling to identify the large-scale circulation patterns associated with 1097  
3 1051 heavy precipitation events over southern France. *Quart. J. R. Meteorol.*  
4 1052 *Soc.*, **137**, 18121827, doi:10.1002/qj.866. 1098  
5 1053 Pastor, F., M. J. Estrela, P. Penarrocha, and M. M. Millan, 2001: Torrential 1100  
6 1054 rains on the spanish Mediterranean coast: Modelling the effect of the sea 1101  
7 1055 surface temperature. *J. Appl. Meteorol.*, **40**, 1180-1195. 1102  
8 1056 Pinty, J.-P., and P. Jabouille, 1998: A mixed-phased cloud parameterization 1103  
9 1057 for use in a mesoscale non-hydrostatic model: Simulations of a squall line 1104  
10 1058 and of orographic precipitation. Preprints, *Conf. on Cloud Physics*, Everett, 1105  
11 1059 WA, Amer. Meteor. Soc., 217-220. 1106  
12 1060 Pullen J., Doyle J. D., Signell R. P., 2006: Two-Way Air-Sea Coupling: A Study 1107  
13 1061 of the Adriatic. *Mon. Wea. Rev.*, **134**, 1465-1483, doi:10.1175/MWR3137.1. 1108  
14 1062 Pullen J., Doyle J. D., Haack T., Dorman C., Signell R. P., Lee C. M.; 2007: 1109  
15 1063 Bora event variability and the role of air-sea feedback. *J. Geophys. Res.*, 1110  
16 1064 **112** (C3), 1-17, doi:10.1029/2006JC003726. 1111  
17 1065 Rainaud, R., 2015: "Modélisation couplée océan-atmosphère pour l'étude des 1112  
18 1066 événements météorologiques intenses en Méditerranée occidentale". PhD 1113  
19 1067 thesis. In french: *University Toulouse III, Paul Sabatier*, 218pp. 1114  
20 1068 Rainaud, R., Lebeauin Brossier C., Ducrocq V., Giordani H., Nuret 1115  
21 1069 M., Fourrié N., Bouin M-N., Taupier-Letage I., Legain D., 2016: 1116  
22 1070 Characterisation of air-sea exchanges over the Western Mediterranean Sea 1117  
23 1071 during the HyMeX SOP1 using the AROME-WMED model. *Quart. J. Roy.*  
24 1072 *Meteorol. Soc.*, **142** (S1), 173-187, doi:10.1002/qj.2480. 1118  
25 1073 Renault L., Chiggiato J., Warner J. C., Gomez M., Vizoso G., Tintore 1119  
26 1074 J., 2012: Coupled atmosphere-ocean-wave simulations of a storm event 1120  
27 1075 over the Gulf of Lion and Balearic Sea. *J. Geophys. Res.*, **117**, C09019, 1121  
28 1076 doi:10.1029/2012JC007924. 1122  
29 1077 Ricard, D., Ducrocq V., Auger L., 2012: A climatology of the mesoscale 1123  
30 1078 environment associated with heavily precipitating events over the 1124  
31 1079 Northwestern Mediterranean area. *J. Appl. Meteorol. Clim.*, **51**, 468-488. 1125  
32 1080 Ricchi, A., M. M. Miglietta, P. P. Falco, A. Benetazzo, D. Bonaldo, 1126  
33 1081 A. Bergamasco, M. Sclavo, S. Carniel, 2016: On the use of 1127  
34 1082 a coupled ocean-atmosphere-wave model during an extreme cold 1128  
35 1083 air outbreak over the Adriatic Sea. *Atmos. Res.*, **172-173**, 48-65, 1129  
36 1084 doi:10.1016/j.atmosres.2015.12.023. 1130  
37 1085 Romero, R., Ramis C., Alonso S., Doswell C. A., Stenrud D. J., 1998: 1131  
38 1086 Mesoscale model simulations of three heavy precipitation events in the 1132  
39 1087 Western Mediterranean region. *Mon. Wea. Rev.*, **126** (7), 1859-1881. 1133  
40 1088 Romero, R., C. Ramis, V. Homar, 2015: On the severe convective storm of 29 1134  
41 1089 October 2013 in the Balearic Islands: observational and numerical study. 1135  
42 1090 *Quart. J. Roy. Meteorol. Soc.*, **141**, 1208-1222, doi:10.1002/qj.2429. 1136  
43 1091 Rouillet G., Madec G., 2000: Salt conservation, free surface, and varying levels: 1137  
44 1092 A new formulation for ocean general circulation models. *J. Geophys. Res.*, 1138  
45 1093 **105** (C10), 23927-23942, doi:10.1029/2000JC900089. 1139  
46 1094 Seity Y., Brousseau P., Malardel S., Hello G., Bénard P., Bouttier F., Lac 1140  
47 1095 C., Masson V., 2011: The AROME-France Convective-Scale Operational 1141  
48 1096 Model. *Mon. Wea. Rev.*, **139**, 976-991. 1142  
49 1097 Silvestro, F., Gabellani S., Giannoni F., Parodi A., Rebora N., Rudari R., 1143  
50 1098 Siccardi F., 2012: A hydrological analysis of the 4 november 2011 event 1144  
51 1099 in genoa. *Nat. Haz. Earth Sys. Sci.*, **12** (9), 2743-2752. 1145  
52 1100 Small R., Campbell T., Teixeira J., Carniel S., Smith T., Dykes J., Chen S., 1146  
53 1101 Allard R., 2011: Air-sea interaction in the Ligurian Sea: Assessment of a 1147  
54 1102 Coupled Ocean-Atmosphere Model using in situ data from LASIE07. *Mon.*  
55 1103 *Wea. Rev.*, **139** (6), 1785-1808, doi:10.1175/2010MWR3431.1. 1148  
56 1104 Small R., Carniel S., Campbell T., Teixeira J., Allard R., 2012: The 1149  
57 1105 response of the Ligurian and Tyrrhenian Seas to a summer Mistral 1150  
58 1106 event: A coupled atmosphere-ocean approach. *Ocean Model.*, **48**, 30-44, 1151  
59 1107 doi:10.1016/j.ocemod.2012.02.003. 1152  
60 1108 Stocchi, P. and Davolio, S., 2016: Intense air-sea exchanges and heavy 1153  
1109 rainfall: impact of the northern Adriatic SST. *Adv. Sci. Res.*, **13**, 7-12, 1154  
1110 doi:10.5194/asr-13-7-2016. 1155  
1111 Taillefer, F., 2002: CANARI (Code for the Analysis Necessary for 1112  
1112 Arpege, for its Rejects and its Initialization): Technical documenta- 1113  
1113 tion. *Technical report*, Groupe de Modélisation pour l'Assimilation 1114  
1114 et la Prévision, Centre National de Recherches Météorologiques, 1115  
1115 Météo-France, Toulouse, France. [http://www.crn.meteo.fr/](http://www.crn.meteo.fr/gmapdoc/spip.php?article3) 1116  
1116 [gmapdoc/spip.php?article3](http://www.crn.meteo.fr/gmapdoc/spip.php?article3). 1117  
1117 Thévenot, O., M-N. Bouin, V. Ducrocq, C. Lebeauin Brossier, O. Nuissier, J. 1118  
1118 Pianezze, F. Duffourg, 2016: Influence of the sea state on Mediterranean 1119  
1119 heavy precipitation: a case study from HyMeX SOP1. *Quart. J. Roy.*  
1120 *Meteorol. Soc.*, **142** (S1), 377-389, doi:10.1002/qj.2660. 1121  
1121 Valcke, S., 2013: The OASIS3 coupler: a European climate modelling 1122  
1122 community software. *Geosci. Model Dev.*, **6**, 373-388, doi:10.5194/gmd- 1123  
1123 6-373-2013. 1124  
1124 Voltaire, A., B. Decharme, J. Pianezze, C. Lebeauin Brossier, F. Sevault, L. 1125  
1125 Seyfried, V. Garnier, S. Bielli, S. Valcke, A. Alias, M. Accensi, F. Arduin, 1126  
1126 M-N. Bouin, V. Ducrocq, S. Faroux, H. Giordani, F. Léger, P. Marsaleix, R. 1127  
1127 Rainaud, J.-L. Redelsperger, E. Richard, S. Riette, 2017: The seamless and 1128  
1128 multi-model coupling between atmosphere, land, hydrology, ocean, waves 1129  
1129 and sea-ice models based on SURFEX surface model using OASIS3-MCT. 1130  
1130 *Geosci. Model Dev. Disc.*, doi:10.5194/gmd-2017-91. 1131  
1131 Warner, J. C., Armstrong B., He R., Zambon J. B., 2010: Development of a 1132  
1132 coupled ocean-atmosphere-wave-sediment transport (COAWST) modeling 1133  
1133 system. *Ocean Model.*, **35** (3), 230-244. 1134  
1134 Xie S. P., Xu H. M., Kessler W. S., Nonaka M., 2005: Air-sea interaction 1135  
1135 over the eastern pacific warm pool: Gap winds, thermocline dome, and 1136  
1136 atmospheric convection. *J. Clim.*, **18** (1), 5-20. 1137

1  
2  
3  
4  
5  
6  
7  
8  
9  
10  
11  
12  
13  
14  
15  
16  
17  
18  
19  
20  
21  
22  
23  
24  
25  
26  
27  
28  
29  
30  
31  
32  
33  
34  
35  
36  
37  
38  
39  
40  
41  
42  
43  
44  
45  
46  
47  
48  
49  
50  
51  
52  
53  
54  
55  
56  
57  
58  
59  
60

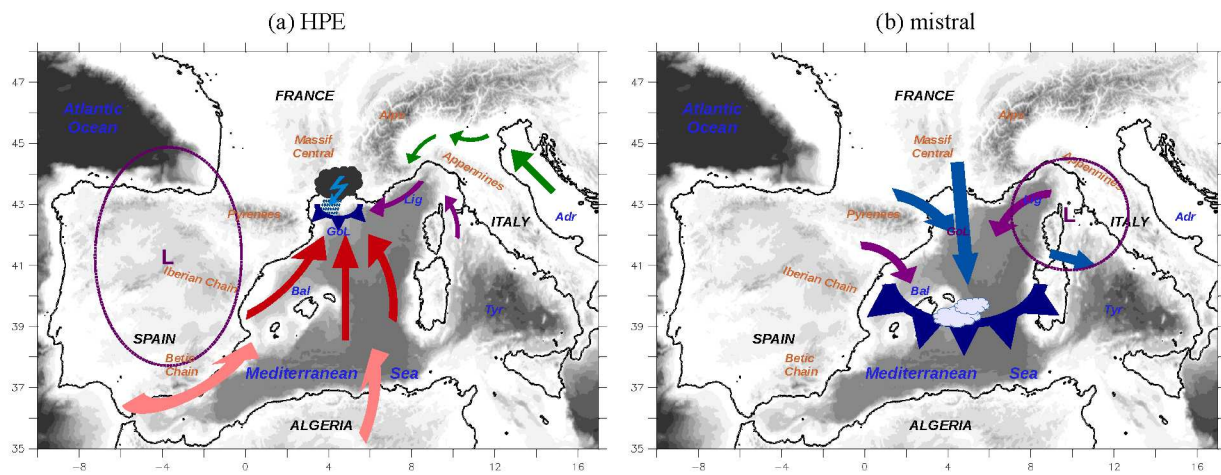


**Figure 1.** Schematic view of the low-level atmospheric circulation over the Western Mediterranean area: (a) during a HPE over South-Eastern France adapted from Ducrocq et al. (2016). The arrows represent the low-level circulation, the darkblue line with triangles represents the cold pool beneath the convective system. The location of the surface low pressure is indicated by the "L-ellipse"; (b) during a mistral/tramontane event. The location of the surface low pressure is indicated by the "L-ellipse". Convection often occur at the lee of the strong wind symbolized by a cold front represented by the darkblue line with triangles.

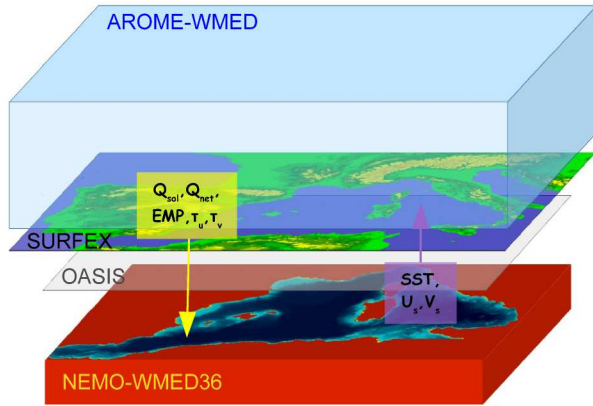


Figure 2. Architecture and domain of the AROME-NEMO WMED coupled system.

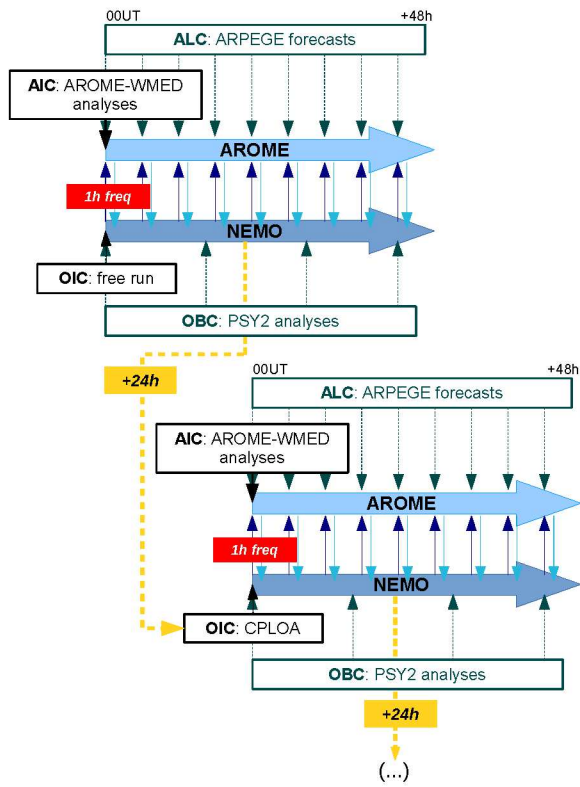


Figure 3. Numerical setup for the CPLOA experiment. ALC [OBC] stands for Atmospheric [Ocean] Lateral [Boundary] Conditions and AIC [OIC] for Atmospheric [Ocean] Initial Conditions.

1  
2  
3  
4  
5  
6  
7  
8  
9  
10  
11  
12  
13  
14  
15  
16  
17  
18  
19  
20  
21  
22  
23  
24  
25  
26  
27  
28  
29  
30  
31  
32  
33  
34  
35  
36  
37  
38  
39  
40  
41  
42  
43  
44  
45  
46  
47  
48  
49  
50  
51  
52  
53  
54  
55  
56  
57  
58  
59  
60

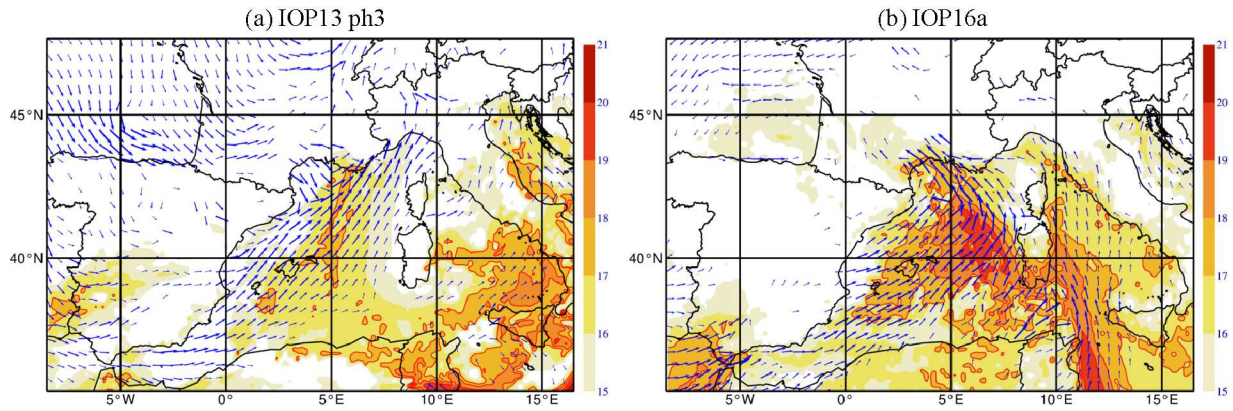


Figure 4. Wet-bulb temperature  $\theta'_w$  (colors, in  $^{\circ}\text{C}$ ) and wind (arrows, above  $5\text{ m s}^{-1}$ ) at 950 hPa in AROME-WMED real-time forecasts: (a) for 14 September 2012 18UTC - IOP13 phase 3 (forecast basis: 14 September 2012 00UTC; range: +18h) and (b) for 26 September 2012 09UTC - IOP16a (forecast basis: 26 September 2012 00UTC; range: +9h). Source: <http://hoc.sedoo.fr>.

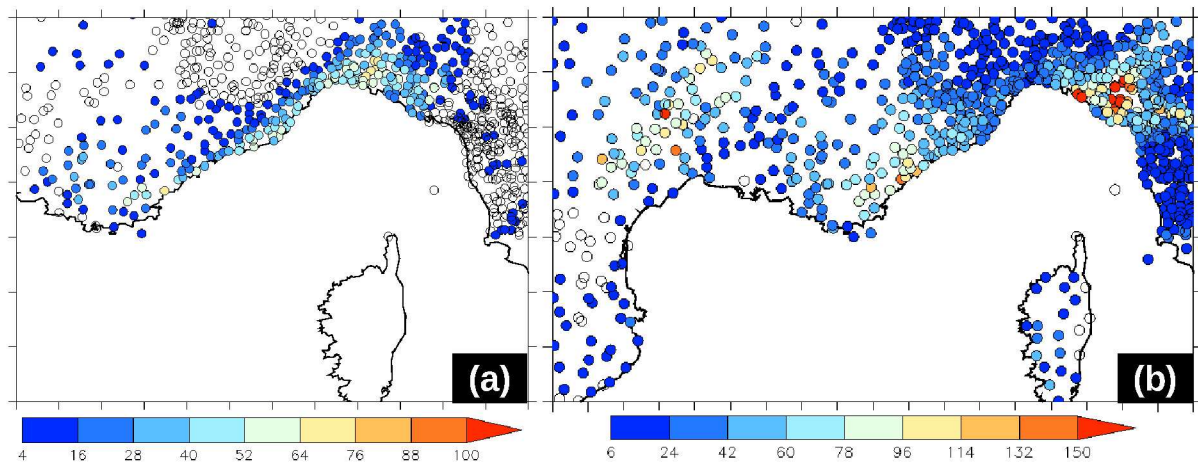
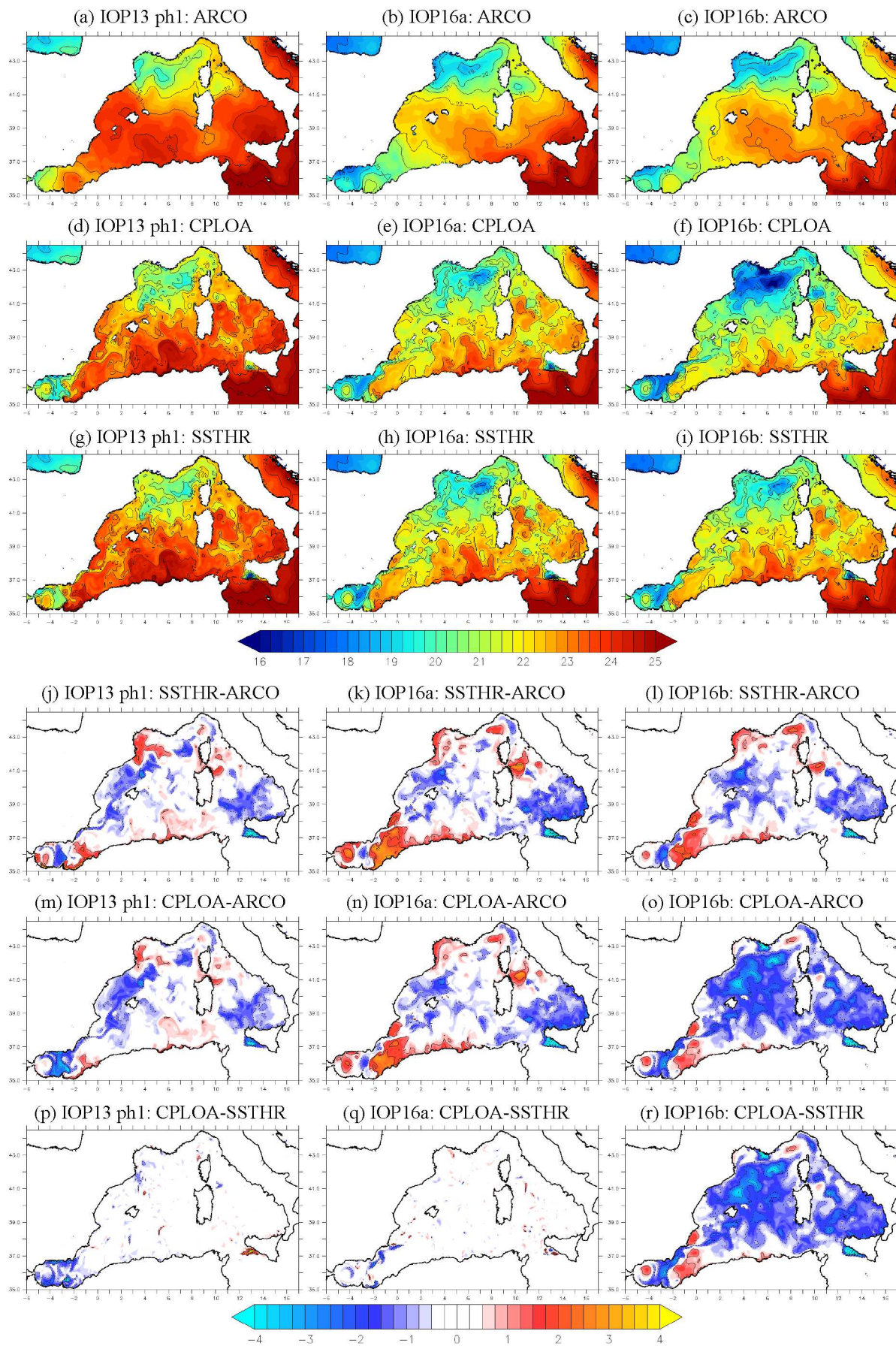


Figure 5. Daily-accumulated precipitation amounts (mm) from rain-gauges: (a) for 14 October 2012 (IOP13 phase 3) and (b) for 26 October 2012 (IOP16a).

1  
2  
3  
4  
5  
6  
7  
8  
9  
10  
11  
12  
13  
14  
15  
16  
17  
18  
19  
20  
21  
22  
23  
24  
25  
26  
27  
28  
29  
30  
31  
32  
33  
34  
35  
36  
37  
38  
39  
40  
41  
42  
43  
44  
45  
46  
47  
48  
49  
50  
51  
52  
53  
54  
55  
56  
57  
58  
59  
60

1  
2  
3  
4  
5  
6  
7  
8  
9  
10  
11  
12  
13  
14  
15  
16  
17  
18  
19  
20  
21  
22  
23  
24  
25  
26  
27  
28  
29  
30  
31  
32  
33  
34  
35  
36  
37  
38  
39  
40  
41  
42  
43  
44  
45  
46  
47  
48  
49  
50  
51  
52  
53  
54  
55  
56  
57  
58  
59  
60



**Figure 6.** SST (°C) for 13 October 00UTC (IOP13 phase 1 - forecast basis: 11 October 2012; range: +48h) [left panels], for 27 October 00UTC (IOP16a - forecast basis: 25 October 2012; range: +48h) [middle panels] and for 29 October 00UTC (IOP16b - forecast basis: 27 October 2012; range: +48h) [right panels] for ARCO (a,b,c) CPLOA (d,e,f) and SSTHR (g,h,i) experiments. Differences in SST (°C): SSTHR minus ARCO (j,k,l); CPLOA minus ARCO (m,n,o) and CPLOA minus SSTHR (p,q,r) for 13 October 00UTC (IOP13 phase 1 - forecast basis: 11 October 2012; range: +48h) [left panels], for 27 October 00UTC (IOP16a - forecast basis: 25 October 2012; range: +48h) [middle panels] and for 29 October 00UTC (IOP16b - forecast basis: 27 October 2012; range: +48h) [right panels].

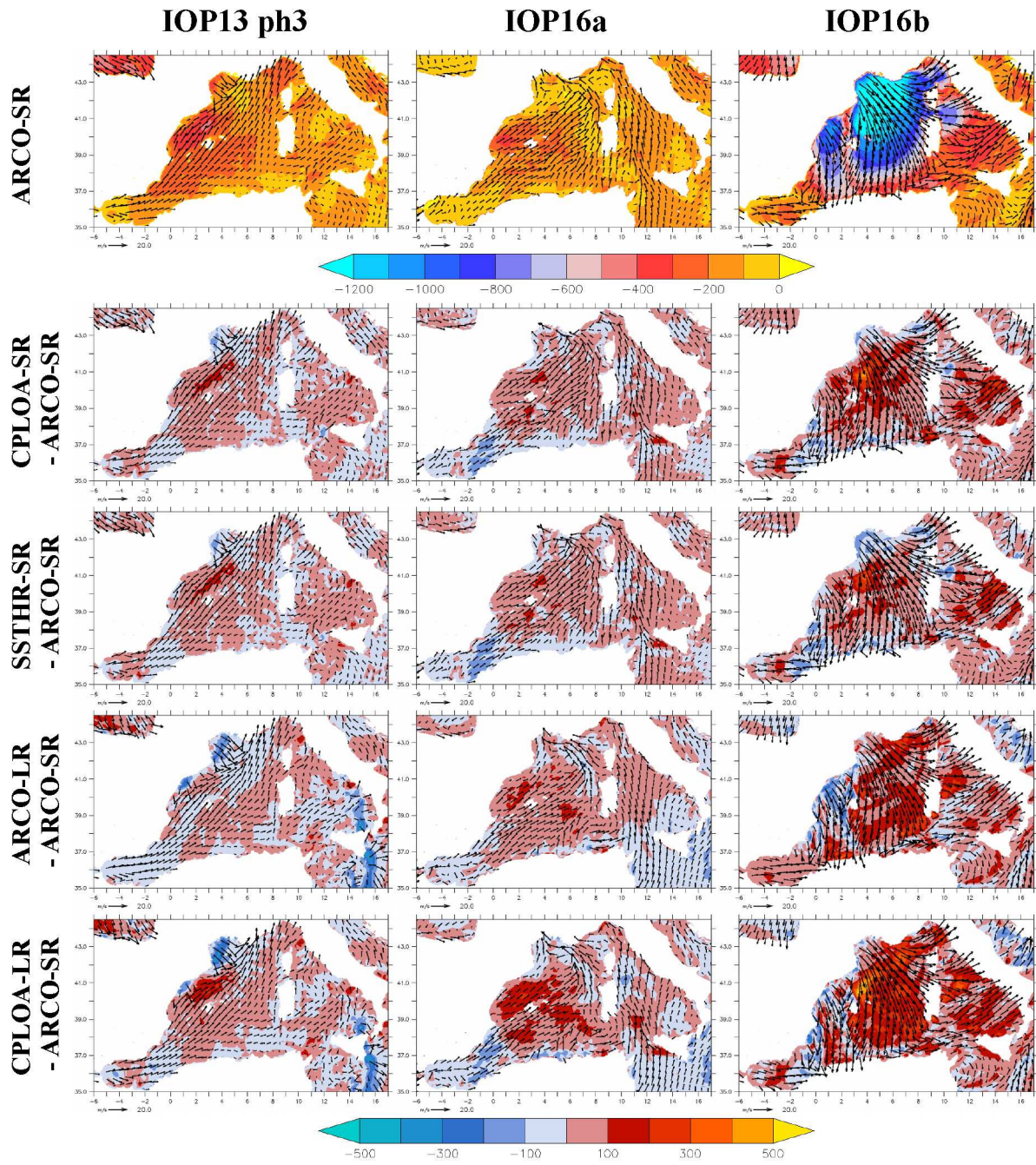


**Figure 7.** First line: Total turbulent heat flux ( $W m^{-2}$ ) and wind ( $m s^{-1}$ ) at first level of the AROME-WMED model ( $\sim 10$  m-height) in ARCO-SR. Differences in total heat flux with ARCO-SR and forecast of the wind at first level for CPLOA-SR [second line], SSTHR-SR [third line], ARCO-LR [fourth line] and CPLOA-LR [ffifth line]; for IOP13 phase 3 (14 October 18UTC) [left], IOP16a (26 October 12UTC) [middle] and IOP16b (28 October 00UTC) [right].



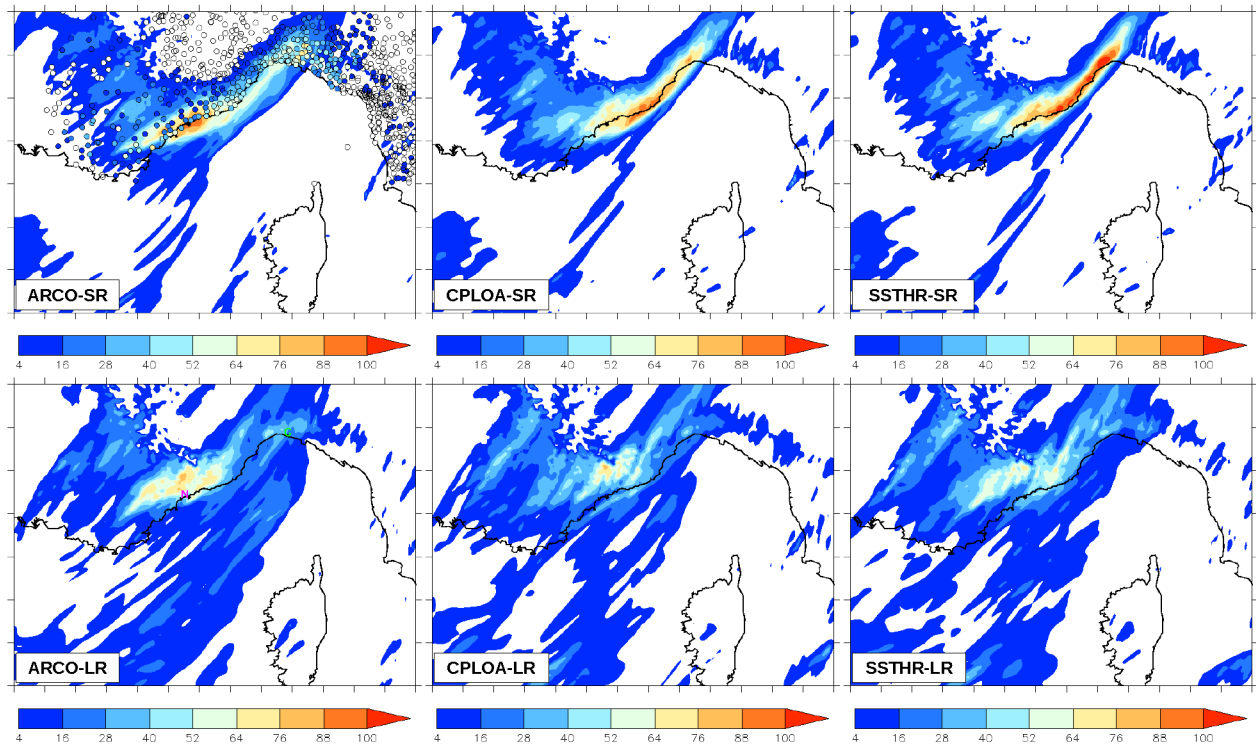


**Figure 8.** Accumulated rainfall (mm) from 14 October 16UTC to 15 October 00UTC (forecast basis: 14 October 2012 00UT [*top panels*] and 13 October 2012 00UT [*bottom panels*]) for ARCO [*left*], CPLOA [*middle*] and SSTHR [*right*] experiments. In the upper left panel, the colored circles correspond to the daily-accumulated precipitation amounts (mm) for 14 October 2012 from rain-gauges (See also Fig. 5a). In the lower left panels, the purple "N" indicates Nice location; the green "G" indicates Genoa location.

1  
2  
3  
4  
5  
6  
7  
8  
9  
10  
11  
12  
13  
14  
15  
16  
17  
18  
19  
20  
21  
22  
23  
24  
25  
26  
27  
28  
29  
30  
31  
32  
33  
34  
35  
36  
37  
38  
39  
40  
41  
42  
43  
44  
45  
46  
47  
48  
49  
50  
51  
52  
53  
54  
55  
56  
57  
58  
59  
60

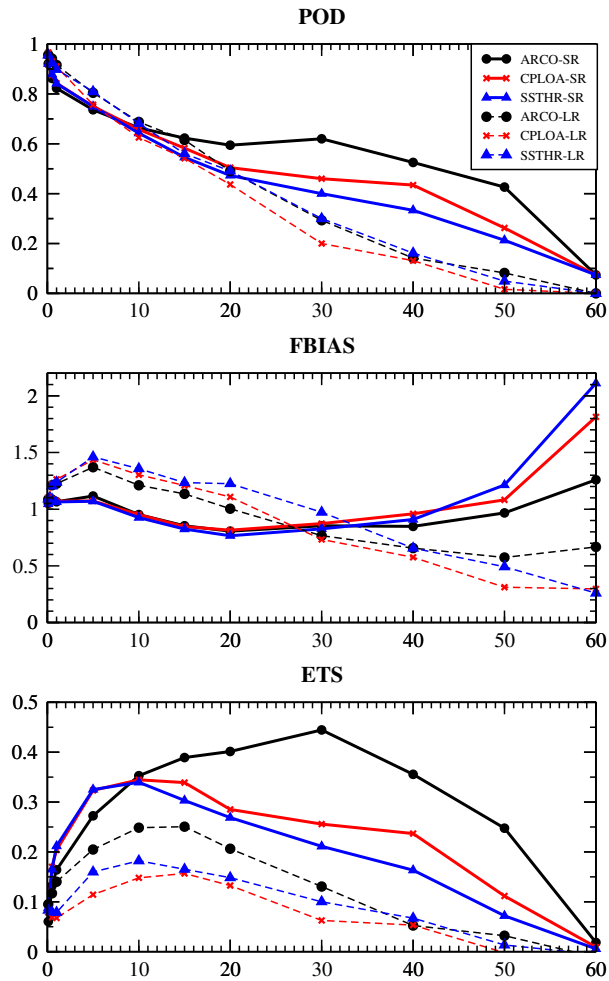
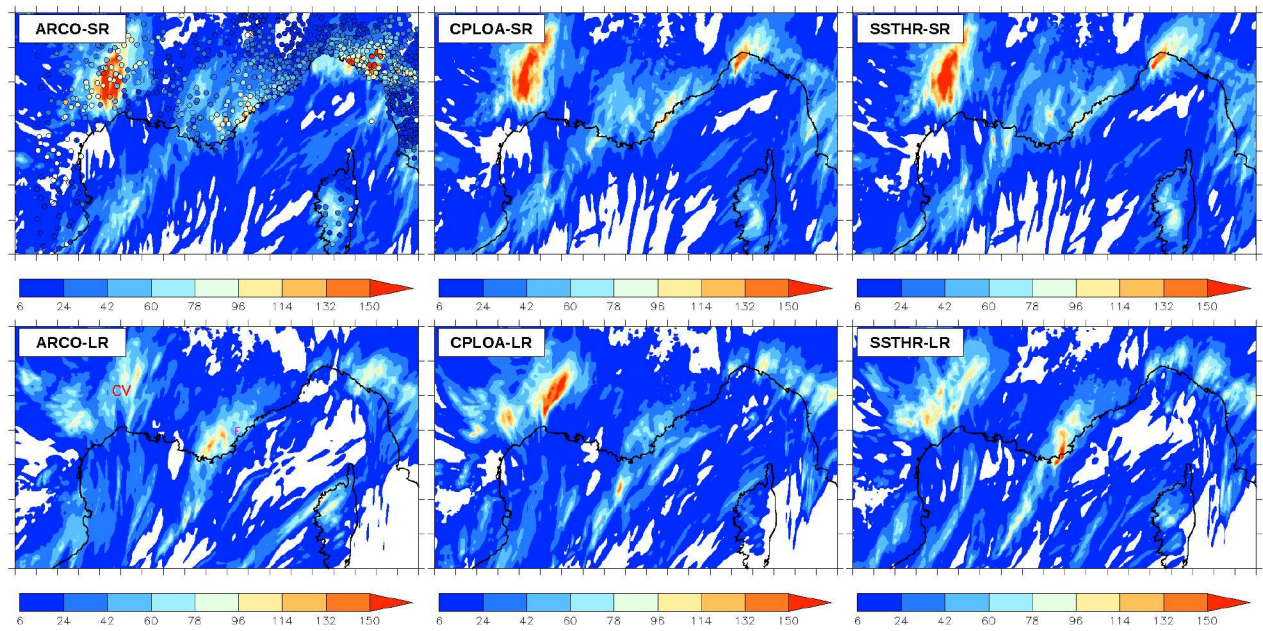


Figure 9. Probability of detection (POD), frequency bias (FBIAS) and equitable threat score (ETS) as a function of a considered threshold for the 24h-accumulated rainfall (mm) from 14 October 00UTC to 15 October 00UTC (forecast basis: 14 October 2012 00UT for SR experiments and 13 October 2012 00UT for LR experiments). A perfect forecast has FBIAS, POD and ETS equal to 1.



**Figure 10.** Accumulated rainfall (mm) from 26 October 00UTC to 27 October 00UTC (forecast basis: 26 October 2012 00UT [*top panels*] and 25 October 2012 00UT [*bottom panels*]) for ARCO [*left*], CPLOA [*middle*] and SSTHR [*right*] experiments. In the upper left panel, the colored circles correspond to the daily-accumulated precipitation amounts (mm) for 26 October 2012 from rain-gauges (See also Fig. 5b). In the lower left panels, the purple "F" indicates Frejus (Var) location; the red "CV" indicates the Cévennes area.

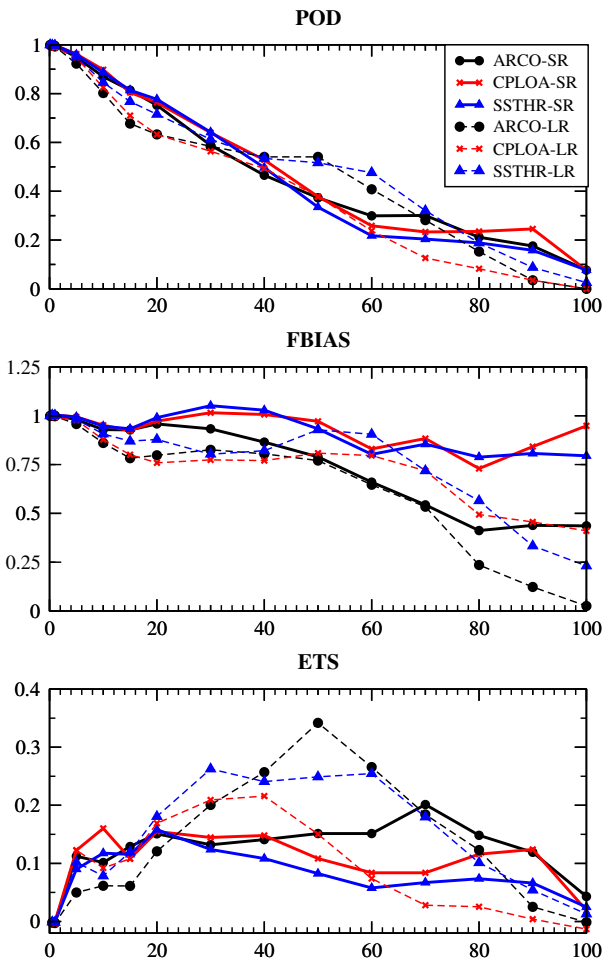


Figure 11. As Fig. 9 but considering the 24h-accumulated rainfall (mm) from 26 October 00UTC to 27 October 00UTC (forecast basis: 26 October 2012 00UT for SR experiments and 25 October 2012 00UT for LR experiments).

Pre-Review

1  
2  
3  
4  
5  
6  
7  
8  
9  
10  
11  
12  
13  
14  
15  
16  
17  
18  
19  
20  
21  
22  
23  
24  
25  
26  
27  
28  
29  
30  
31  
32  
33  
34  
35  
36  
37  
38  
39  
40  
41  
42  
43  
44  
45  
46  
47  
48  
49  
50  
51  
52  
53  
54  
55  
56  
57  
58  
59  
60

1  
2  
3  
4  
5  
6  
7  
8  
9  
10  
11  
12  
13  
14  
15  
16  
17  
18  
19  
20  
21  
22  
23  
24  
25  
26  
27  
28  
29  
30  
31  
32  
33  
34  
35  
36  
37  
38  
39  
40  
41  
42  
43  
44  
45  
46  
47  
48  
49  
50  
51  
52  
53  
54  
55  
56  
57  
58  
59  
60

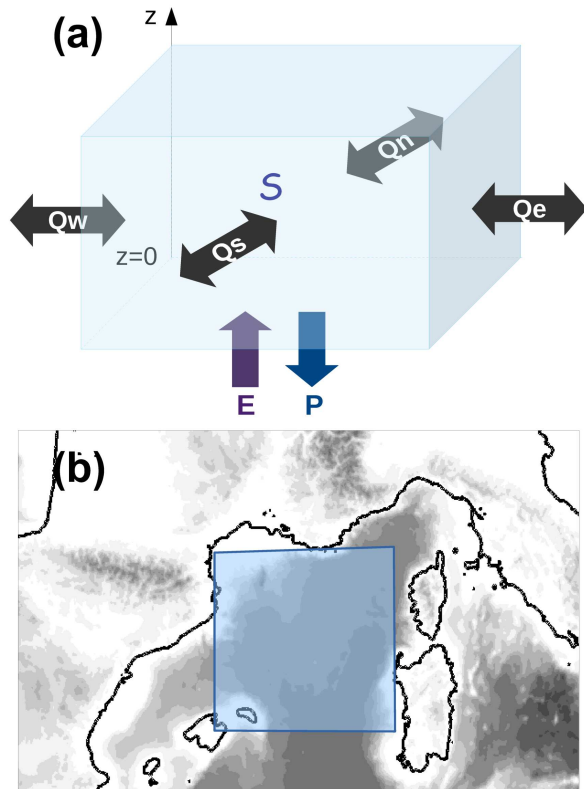
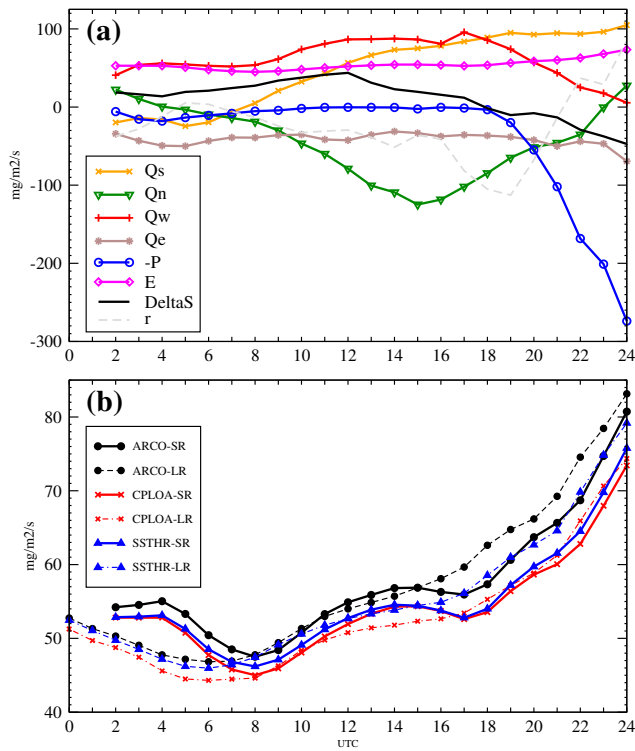


Figure 12. (a) Scheme of the water content budget and components:  $S$  is the storage of total atmospheric water within the budget box,  $E$  is the surface evaporation,  $P$  precipitation and  $Q_n$ ,  $Q_e$ ,  $Q_s$ ,  $Q_w$  are the vertically integrated horizontal fluxes of water through the four sides of the box. (b) Budget box location.

Pre Review

1  
2  
3  
4  
5  
6  
7  
8  
9  
10  
11  
12  
13  
14  
15  
16  
17  
18  
19  
20  
21  
22  
23  
24  
25  
26  
27  
28  
29  
30  
31  
32  
33  
34  
35  
36  
37  
38  
39  
40  
41  
42  
43  
44  
45  
46  
47  
48  
49  
50  
51  
52  
53  
54  
55  
56  
57  
58  
59  
60



**Figure 13.** (a) Water budget components ( $\text{mg m}^{-2} \text{s}^{-1}$ ) in CPLOA for IOP13 phase 3 (14 October 2012, forecast basis: 14 October 00UTC) for the low levels (0 - ~500 m) [see the box in Fig. 12]. (b) Evaporation contribution ( $\text{mg m}^{-2} \text{s}^{-1}$ ) to water budget for 14 October 2012 in ARCO, CPLOA, and SSTHR for SR forecast (forecast basis: 14 October 00UTC) and LR forecast (forecast basis: 13 October 00UTC).

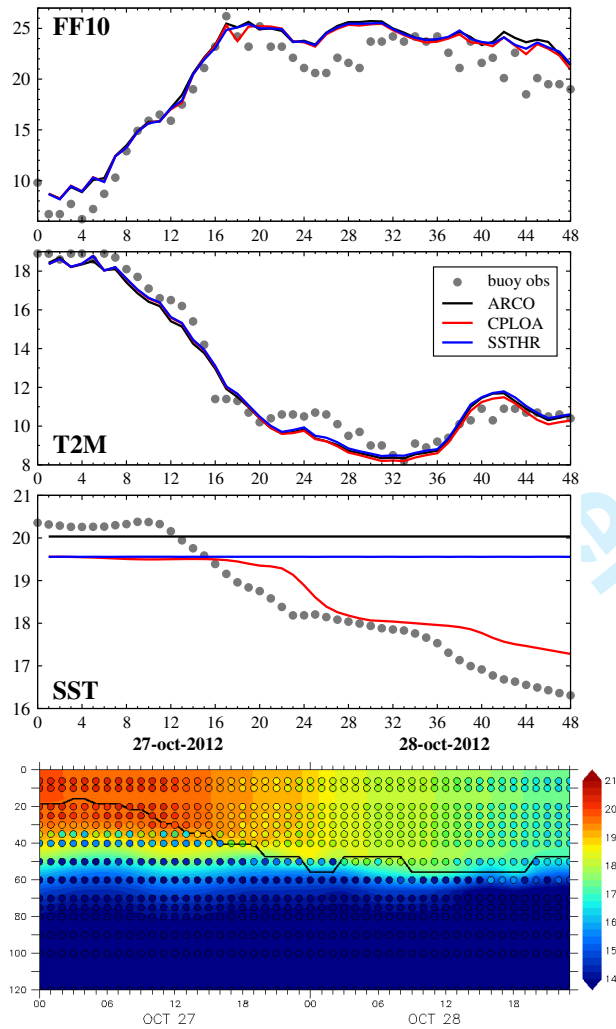


**Figure 14.** IOP16b (27-28 October 2012) at the LION buoy: [top panels] Time-series of 10m-wind speed (FF10,  $\text{m s}^{-1}$ ), 2m-temperature (T2M,  $^{\circ}\text{C}$ ) and SST ( $^{\circ}\text{C}$ ) for ARCO (black), CPLOA (red) and SSTHR (blue) (forecast basis: 27 October 2012 00UT. Observations are the grey circles. [bottom panel] Time-series of the ocean temperature ( $^{\circ}\text{C}$ ) profile simulated by CPLOA. The black line indicates the simulated MLD from a density criterion. The circles are observations from the bathymetric thermistance chain.

Pre-Review

Table 1. Bias (mm), Root Mean Squared Error (RMSE, mm) and correlation (CORR) for the simulated 24h-cumulated rainfall amounts on 14 October 2012 against raingauge observations.

	<i>SR</i>		
	ARCO	CPLOA	SSTHR
BIAS	-0.426	0.018	0.537
RMSE	14.235	16.394	18.646
CORR	0.662	0.586	0.538
	<i>LR</i>		
	ARCO	CPLOA	SSTHR
BIAS	0.719	0.862	1.768
RMSE	16.934	18.461	18.306
CORR	0.464	0.321	0.365

Table 2. As Table 1 but for the simulated 24h-cumulated rainfall amounts on 26 October 2012.

	<i>SR</i>		
	ARCO	CPLOA	SSTHR
BIAS	-4.967	-1.760	-1.648
RMSE	29.872	33.688	34.610
CORR	0.450	0.334	0.291
	<i>LR</i>		
	ARCO	CPLOA	SSTHR
BIAS	-8.864	-7.614	-6.271
RMSE	26.435	31.860	28.444
CORR	0.590	0.400	0.500

Table A. Schematic  $2 \times 2$  contingency table for the definition of scores, given a threshold *thr* for the rainfall amount.

	simulation < <i>thr</i>	simulation $\geq$ <i>thr</i>
observation < <i>thr</i>	a	b
observation $\geq$ <i>thr</i>	c	d